J. Fluid Mech. (1989), *vol.* 206, *pp.* 299–338
Printed in Great Britain

Optical and acoustic investigations of the dynamics of laser-produced cavitation bubbles near a solid boundary

By A. VOGEL†, W. LAUTERBORN‡ AND R. TIMM‖
Drittes Physikalisches Institut, University of Göttingen, Federal Republic of Germany

(Received 11 May 1988 and in revised form 18 November 1988)

The dynamics of laser-produced cavitation bubbles near a solid boundary and its dependence on the distance between bubble and wall are investigated experimentally. It is shown by means of high-speed photography with up to 1 million frames/s that jet and counterjet formation and the development of a ring vortex resulting from the jet flow are general features of the bubble dynamics near solid boundaries. The fluid velocity field in the vicinity of the cavitation bubble is determined with time-resolved particle image velocimetry. A comparison of path lines deduced from successive measurements shows good agreement with the results of numerical calculations by Kucera & Blake (1988). The pressure amplitude, the profile and the energy of the acoustic transients emitted during spherical bubble collapse and the collapse near a rigid boundary are measured with a hydrophone and an optical detection technique. Sound emission is the main damping mechanism in spherical bubble collapse, whereas it plays a minor part in the damping of aspherical collapse. The duration of the acoustic transients is 20–30 ns. The highest pressure amplitudes at the solid boundary have been found for bubbles attached to the boundary. The pressure inside the bubble and at the boundary reaches about 2.5 kbar when the maximum bubble radius is 3.5 mm. The results are discussed with respect to the mechanism of cavitation erosion.

1. Introduction

Historically, the interest in the dynamics of cavitation bubbles in liquids mainly arose from their destructive action on solid surfaces, which has been observed on ship propellers and in hydraulic machinery. As recently summarized by Tomita & Shima (1986), cavitation erosion is attributed to the action of acoustic transients emitted during bubble collapse and to the impingement of the high-speed liquid jet that develops when a bubble collapses in the vicinity of a solid boundary. To study the jet formation, Lauterborn (1974) and Lauterborn & Bolle (1975) have produced single cavitation bubbles by focusing Q-switched laser pulses into the liquid under investigation. Thereby plasma formation occurs at the laser focus leading to emission of an acoustic transient and generation of a cavitation bubble (Brewer & Rieckhoff 1964; Carome, Moeller & Clark 1966). Since laser-produced bubbles can be made

† Present address: H. Wacker Laboratory for Medical Laser Applications at the Eye Clinic of the University of Munich, Mathildenstr. 8, 8000 München 2, FRG.
‡ Present address: Institute for Applied Physics, Technische Hochschule Darmstadt, Schloßgartenstr. 7, 6100 Darmstadt, FRG.
‖ Present address: MBB/Erno, Hünefeldstr. 1-5, 2800 Bremen 1, FRG.

highly spherical and are free from mechanical distortions, they meet the requirements necessary for comparing the results of experimental work and numerical investigations. During the few last years, laser-produced cavitation bubbles have also become important in the medical field of ophthalmology and urology. In ocular surgery by means of photodisruption, as introduced by Fankhauser (Fankhauser *et al.* 1981) and Aron-Rosa (Aron-Rosa *et al.* 1980), and in laser-induced lithotripsy (see Steiner 1988), laser pulses are used to produce a plasma with subsequent bubble formation. Tissue disruption and stone fragmentation are related to the mechanism of cavitation erosion, because they are probably due to the combined effects of the plasma, the bubble dynamics and the acoustic transients emitted during bubble generation and collapse (Vogel *et al.* 1986; Reichel *et al.* 1987). Recently, Coleman *et al.* (1987) have demonstrated that cavitation bubble dynamics may also contribute to renal calculi disintegration in extracorporeal shock-wave lithotripsy.

Naudé & Ellis (1961), and Tomita & Shima (1986) have shown that the dynamical behaviour of a bubble strongly depends on the dimensionless distance $\gamma = s/R_{\max}$ between cavitation bubble and wall, with $R_{\max}$ being the maximum bubble radius, and s denoting the distance between the location of bubble formation and the wall. This paper summarizes the results of detailed investigations of jet formation and sound emission as a function of γ. The jet formation has been studied by means of high-speed photography with a framing rate of up to 1 million frames/s. It was shown that over a wide range of the parameter γ a ring vortex emerges from the jet flow, as theoretically predicted by Benjamin & Ellis (1966), and that in a more limited γ-interval a counterjet appears as regularly as the main jet itself. Formerly, only data about the bubble shape had been obtained both experimentally (see Lauterborn & Hentschel 1985) and in numerical model calculations. However, a more detailed investigation of jet formation should include the velocity and pressure field around the bubble. Recently, theory has succeeded in calculating pathlines and pressure contours in the neighbourhood of collapsing bubbles (Blake, Taib & Doherty 1986). By combining particle image velocimetry (PIV) with high-speed photography, we are now able to investigate the temporal development of the unsteady fluid flow around collapsing cavitation bubbles experimentally and to compare it with the numerical results obtained by Kucera & Blake (1988).

In earlier experimental and theoretical work Radek (1972), Hinsch & Brinkmeyer (1976) and Ebeling (1978) found that the pressure pulse emitted upon spherical cavitation bubble collapse has a duration between 10 and 40 ns. Similar values have been reported by Ebeling (1978) and Stepp *et al.* (1985) for the duration of the acoustic transients following laser-induced plasma formation. This is much shorter than the rise time of most calibrated pressure transducers commercially available. Exposing these transducers to the pressure pulses one records merely the impulse response of the transducer, and the indicated pressure values are lower than the actual ones. Transducers with a rise time of a few nanoseconds are, on the other hand, very insensitive and have to be placed close to the centre of the spherical pressure waves. They are not well suited for measuring the sound emission during spherical cavitation bubble collapse, because every boundary in the vicinity of the bubble distorts its dynamics. Therefore, we developed a technique to determine the pressure of short acoustic pulses incorporating a sensitive pressure transducer with a frequency bandwidth smaller than that of the acoustic pulse. For this, the recording of the acoustic signal was combined with a synchronously performed fast optical measurement of the temporal profile of the pressure pulse. From these data, the actual pressure value can be calculated if the transfer function of the transducer is

known. Further processing of the data allows an estimation of the energy of the acoustic transients.

2. Experiments

2.1. *High-speed photography*

Three different experimental arrangements have been used for high-speed photography of laser-produced cavitation bubbles. The basic set-up is outlined in figure 1 (*a*). The bubbles are generated in the cuvette filled with water by using a Q-switched ruby laser which delivers pulses with an energy of 100–400 mJ. The focusing lens has a focal length of 25 mm, and the cone angle of the focused laser beam is 19.5° (in water). The large cone angle was chosen to reduce the probability of generating multiple plasmas by limiting the volume with suprathreshold light intensity. The bubble dynamics is investigated with a drum camera (Impulsphysik model Strobodrum) at 20000 frames/s using diffuse illumination by a flash lamp through a ground glass. The exposure time is set by the spark duration of about 1 μs. The comparatively low framing rate allows the recording of the whole life cycle of the cavity. To study the formation of a ring vortex during bubble collapse, the bubbles were photographed in side view and top view as shown in figure 1 (*b*) and 1 (*c*), respectively. In the arrangement of figure 1 (*b*) a brass block was used as the solid boundary, whereas in 1 (*c*) the cuvette wall served as a transparent rigid boundary.

Figure 2 shows an arrangement for high-speed photography with a schlieren technique. For the determination of the maximum jet velocity one has to know whether it penetrates the opposite bubble wall during collapse or if it merely pushes the wall ahead during rebound. Only in the latter case can the jet velocity be identified with the velocity of the tip of the bubble protrusion observed during rebound by Benjamin & Ellis (1966), and Lauterborn & Bolle (1975). A ring vortex predicted by Benjamin & Ellis (1966) can, on the other hand, only be formed *during* first collapse if the jet penetrates the bubble wall immediately upon impingement. To clarify these questions, we produced the cavitation bubbles within a stationary temperature gradient generated with two Peltier elements as depicted in figure 2 (*b*). The jet penetrating the opposite bubble wall has a different temperature, and therefore a different refractive index than the surrounding liquid. Thus, it becomes a weak phase object and can be visualized by means of a schlieren technique as shown in figure 2 (*a*), though it would be invisible by normal photographic techniques. In the schlieren set-up a flashlamp spark is imaged into the plane of a vertical slit with a width of 40 μm. The illuminating light beam is then collimated and – after passing the cuvette – blocked out with a vertical wire. The wire serves as a high-pass filter for the optical system which images the cavitation bubbles into the film plane of the drum camera. The sensitivity of the apparatus was tested with a model jet from a syringe with a diameter of 0.2 mm (see Vogel & Lauterborn 1985). When the surrounding liquid has a temperature of 273 K (20 °C), a jet with a temperature difference of 0.5 K, corresponding to an optical phase shift of $\lambda/50$, could still be detected. Since the temperature gradient in the cuvette can be adjusted to more than 1 K/mm and the maximum cavitation bubble diameter amounts to some millimetres, the apparatus is sensitive enough to visualize the jet if it pierces the opposite bubble wall.

For studying the bubble dynamics during first collapse with high temporal resolution, we applied a rotating mirror camera (Beckmann and Whitley, model 330) and an image converter camera (Hadland Imacon 790) with a maximum framing

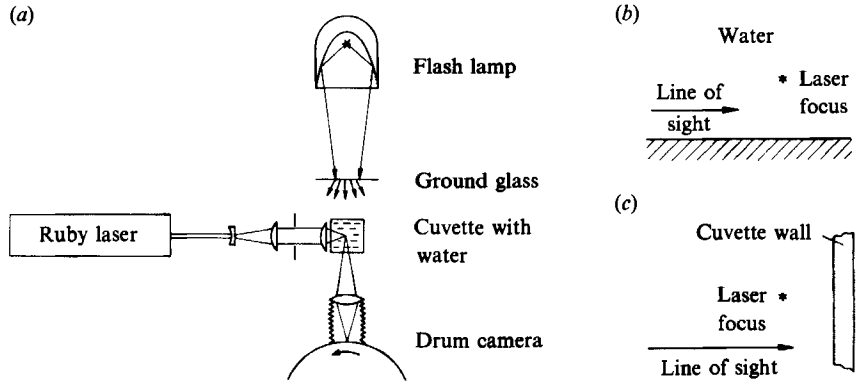

FIGURE 1. (*a*) Basic experimental arrangement for high-speed photography of cavitation bubbles. (*b*, *c*) Principal configurations for the photography of bubble dynamics with the line of sight parallel to the solid wall (*b*) and perpendicular to the solid wall (*c*).

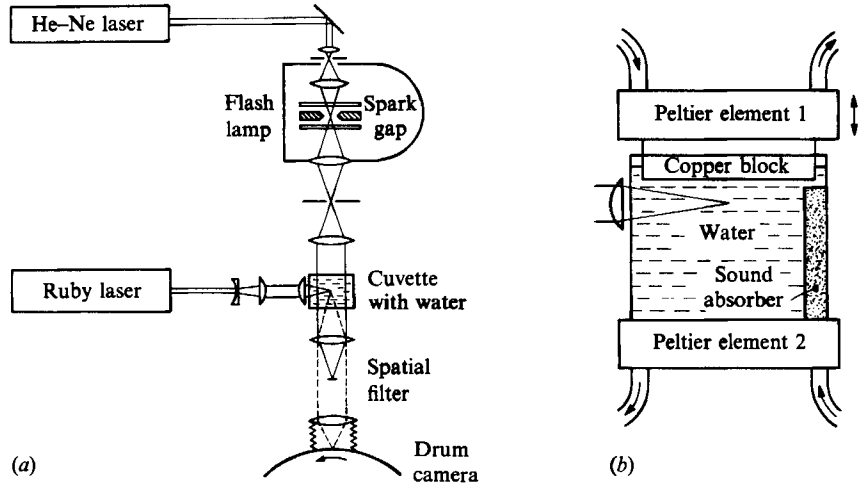

FIGURE 2. (*a*) Experimental arrangement for flow visualization by optical high-pass filtering (schlieren photography). (*b*) Apparatus for the generation of a stationary temperature gradient.

rate of 1 million frames/s. The experimental arrangement is shown in figure 3. To synchronize the photographical recording with the bubble collapse, the camera is triggered by the collapsing cavity itself (Lauterborn & Timm 1980). This is accomplished by letting the cavity modulate the intensity of a helium–neon laser beam which is picked up by a fast photodiode. The laser beam is blocked out when the cavity is expanded. During collapse the light intensity at the diode rises until the cavity reaches its minimum volume. The sudden rise of the diode signal during the final collapse stage triggers the oscilloscope which is used to derive the trigger signal for the camera.

2.2. *Time-resolved particle image velocimetry*

In particle image velocimetry, the fluid is seeded with microparticles serving as light scatterers, the specific gravity of which is chosen to match that of the fluid. A plane in the fluid is illuminated by a thin light sheet, and the particle distribution in this plane is imaged onto photographic film. Since the scattering particles follow the fluid flow, they are recorded as a chain of particle images when the film is multiply

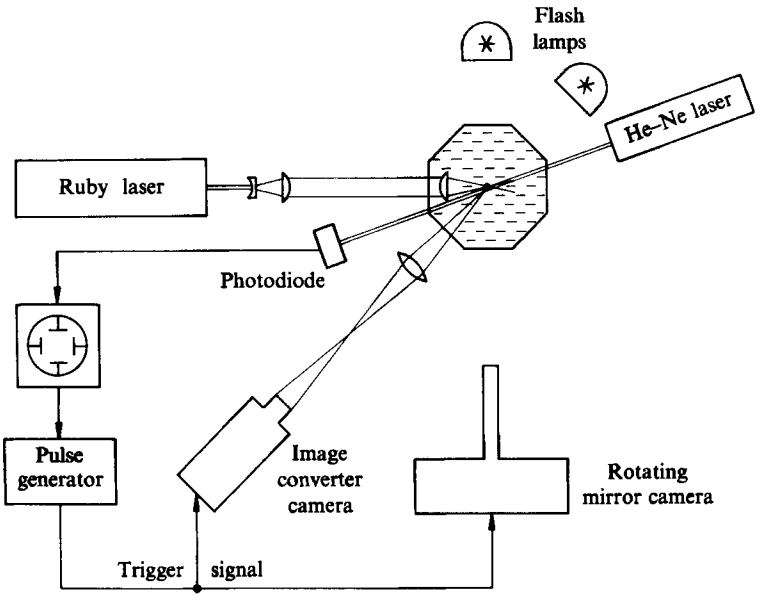

FIGURE 3. Experimental arrangement for high-speed photography with triggering from the cavity itself.

exposed. The projection of the fluid-velocity vector onto the observation plane can be calculated from the direction of each chain, the distance between the particle images and the time between successive exposures. The temporal evolution of the flow field can be monitored by taking a series of multiple exposure photographs. For this, particle image velocimetry and high-speed photography with a drum camera were combined in the experimental arrangement shown in figure 4 (Vogel & Lauterborn 1988*a*). The light source is a 3.6 W argon-ion laser. The laser beam is chopped by an acousto-optic deflector controlled by a cascade of two burst generators. Thus, pulse trains of variable length, pulse separation and repetition rate can be generated. Each frame was exposed with a sequence of five pulses with 1 μs duration and 3 μs distance between successive pulses. The argon laser beam is expanded vertically by a cylindrical lens and focused horizontally by a convex lens to produce a light sheet of 15 mm height and 140 μm thickness in the plane where the centre of the bubble is located. Since the energy of each argon laser pulse is only 3.5 μJ, an imaging system with a large aperture (f-No. 1.25) was chosen to achieve optimum utilization of the scattered light. The water in the cuvette is seeded with Vestamid particles which have an average diameter of 25 μm and a density of 1.01–1.02 g/cm^3. Simultaneously with high-speed photography, both the output signal of the second burst generator and the acoustic signal of the cavitation bubble are recorded with a transient recorder. The first peak of the acoustic signal represents the shock wave emitted during bubble generation, and the following peaks indicate the successive bubble collapses. The output of the burst generator is the driving signal for the illuminating light pulses and marks the instants of film exposure. By comparing both signals, the picture sequence of time-resolved particle image velocimetry can be exactly related to the life cycle of the cavitation bubble. For evaluation, the photographs were magnified and the prints were analysed by individual inspection. With the apparatus described above, fluid velocities can be determined within a range of from less than 2 m/s to 30 m/s. The maximum

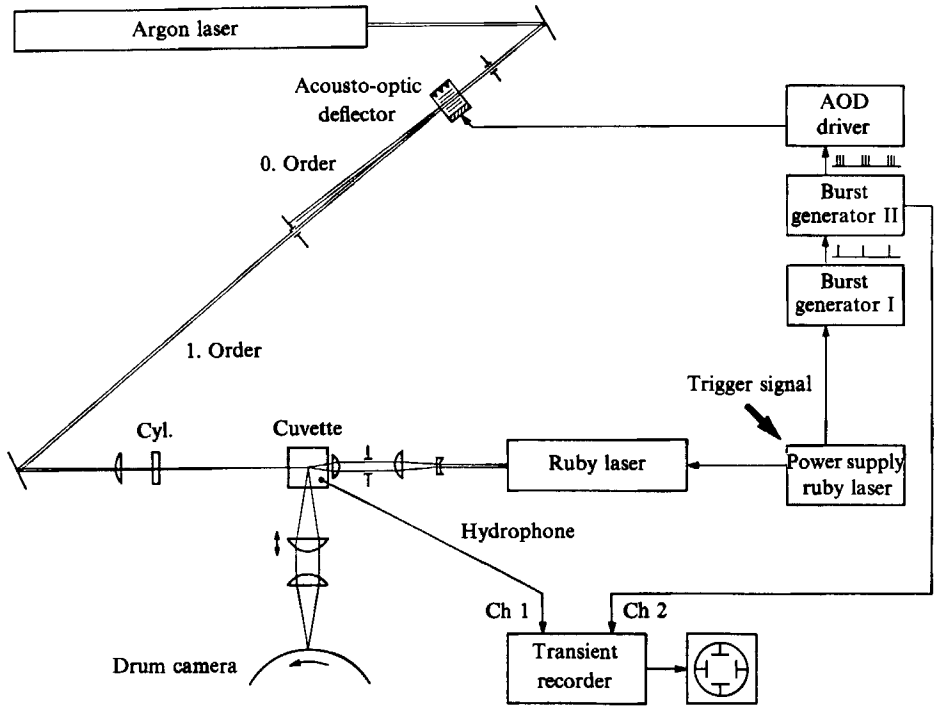

FIGURE 4. Arrangement for time-resolved particle image velocimetry of the flow around laser-produced cavitation bubbles.

temporal resolution achieved is 10000 frames/s and the average density of measurement values is two points/mm^2.

2.3. *Measurement of acoustic pulses*

For calculating the actual values of short pressure pulses from the output signal and the transfer function of the pressure transducer, the temporal profile of the pressure pulse has to be known. As confirmed by the experimental results described below, the profile of the acoustic transients from laser-produced cavitation bubbles can be approximated by an exponential impulse. Vogel & Lauterborn (1988*b*) have shown that the peak amplitude of an exponential pressure pulse is given too low by a factor of

$$m = \frac{\tau}{t_A \ln 2} \tag{1}$$

when the pulse duration τ is much shorter than the rise time t_A of the pressure transducer. In deriving relation (1), the assumption was made that the transfer function of the transducer is constant up to the cutoff frequency $\nu_c = \frac{1}{2}t_A$ and zero for higher frequencies. If τ and t_A are known, (1) yields a correction of the indicated pressure values. The rise time t_A is most conveniently measured when the transducer is hit by a laser-induced acoustic transient with duration $\tau \ll t_A$. The pulse duration τ can be obtained through the optical detection of the temporal profile of the pressure pulses which is a part of the experimental arrangement outlined in figure 5. The probe laser beam from an argon laser is expanded and collimated, and it illuminates the circular aperture 1. The diameter of the aperture is adjusted so that only the central part of the beam with nearly constant intensity can pass. This part is focused

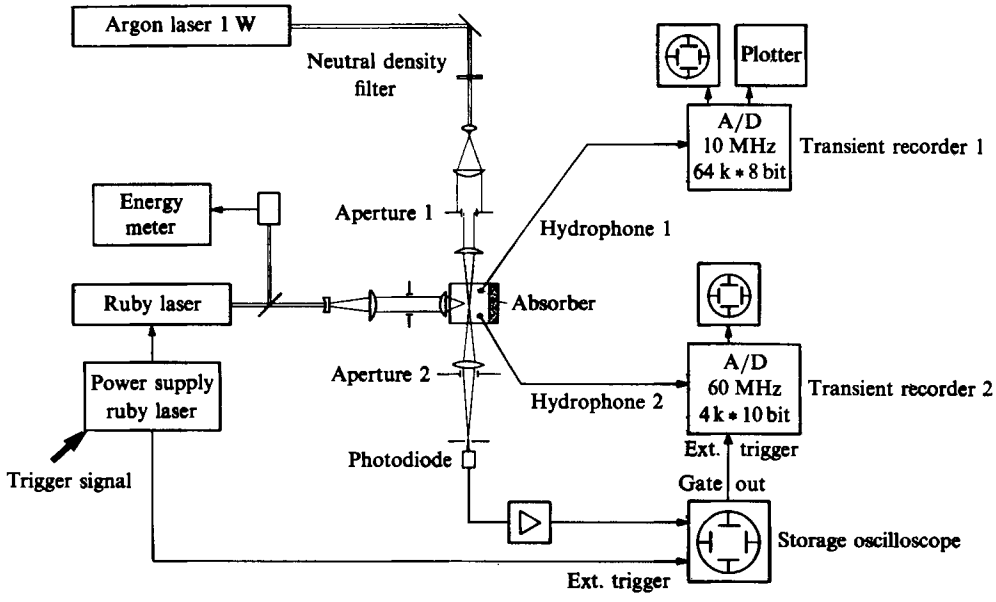

FIGURE 5. Experimental arrangement for the investigation of acoustic transient emission during cavitation-bubble generation and bubble collapse.

into the cuvette close to the emission centre at a radius r_0 of the acoustic transients and the focus is imaged into a small aperture directly in front of a fast photodiode. When an acoustic pulse passes the probe beam waist, a transient angular deflection ϕ of the probe is produced due to the refractive index change caused by the pressure pulse. As a result, the probe beam is partly blocked out by aperture 2 and the intensity of light arriving at the photodiode is modulated. The deflection of the probe beam leads to a reduction of the photodiode voltage U independent of the direction of the deflection so that the voltage is a function of the modulus of the deflection. The $U(\phi)$-characteristic is shown in figure 6 for the theoretical case of a probe beam with a rectangular intensity profile as well as for the experimental apparatus used. In the nearly linear part of the $U(\phi)$-characteristic, the change of the photodiode voltage caused by the pressure wave $p(\boldsymbol{r}, t)$ passing the probe beam focus at $\boldsymbol{r}_0$ can be approximated by

$$U_0 - U(t) \propto \left| \frac{\partial p(\boldsymbol{r}_0, t)}{\partial t} \right|, \tag{2}$$

where U_0 denotes the voltage for $\phi = 0$. Thus, the experimental probe beam deflection signal is proportional to the modulus of the time-derivative of the pressure pulse at the probe beam waist. The temporal resolution of the apparatus described is 10 ns, limited by the time necessary for the pressure pulses to travel through the probe beam focus.

The pressure amplitude of the acoustic transients is determined with hydrophone 1 (Celesco LC5-2) at a distance of about 20 mm from the emission centre (see figure 5). The sensitivity of the transducer is 500 mV/bar and its rise time 333 ns. The transducer signal is registered with 10 MHz sampling rate with transient recorder 1 (Maurer ADAM TC 1008). This instrument has the ability to store 64 k samples with 8 bit resolution, which allows for tracking the sound emission throughout the whole lifetime of the cavitation bubbles. For the optical detection of acoustic transients, the storage oscilloscope is externally pretriggered by a reference pulse from the ruby

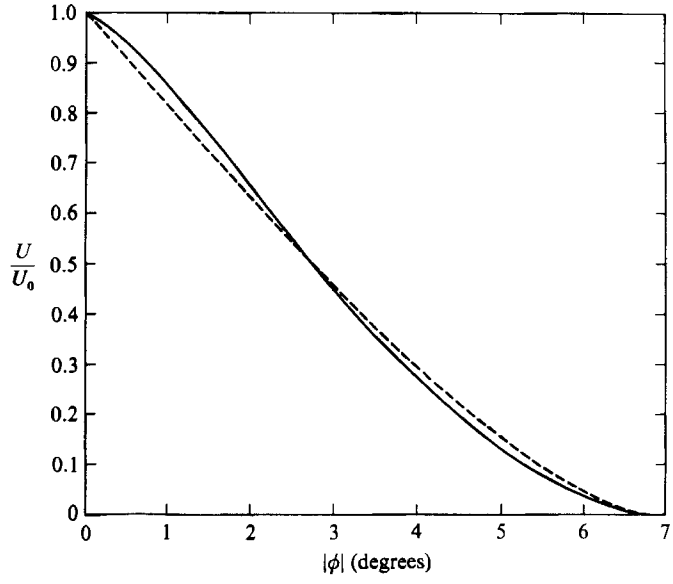

FIGURE 6. The normalized photodiode signal U/U_0 as a function of the angular probe beam deflection ϕ: ----, theoretical curve for homogeneous intensity distribution across the probe beam; ——, curve determined experimentally for the apparatus in figure 5.

laser and then – after an adjustable delay – triggered internally. This method may fail for the relatively weak acoustic pulses emitted after bubble collapse near a solid boundary. Therefore, the correct triggering is checked by coupling the recording of the optical signal with the registration of the acoustical signal by a second pressure transducer (Imotec PVDF pressure gauge) with a rise time of 145 ns, and a sensitivity of about 2.5 mV/bar. Its signal is recorded with 60 MHz sampling rate through transient recorder 2 (Sony/Tektronix 390 A/D). The short rise time of hydrophone 2 allowed, moreover, a less distorted observation of the profile of the acoustic transients than achievable with the more sensitive hydrophone 1.

3. Results

3.1. *Jet formation*

Figure 7 shows several high-speed photographic series of jet formation which illustrate the changes in bubble dynamics with varying distance between bubble and boundary. When the bubble is relatively far away from the solid boundary ($\gamma = 2.3$, figure 7*a*), it migrates toward the boundary during collapse and a jet is developed which leads to the protrusion of the lower bubble wall. The jet is clearly visible in the bright centre of the bubble images. The jet flow creates a ring vortex which is manifested by the continuous migration of the bubble ring toward the boundary (see §3.2). In the second picture series ($\gamma = 1.56$, figure 7*b*), a counterjet appears before the main jet is visible, manifesting itself in the protrusion on the upper bubble side (see §3.3). When γ is smaller than one, no counterjet is observed. With decreasing γ, the jet becomes thicker and touches the lower bubble wall in an earlier stage of the collapse (see also Tomita & Shima 1986). When γ is further reduced, the jet diameter diminishes again as can be seen in figure 7(*d*) with $\gamma = 0.34$.

Fundamental considerations about the mechanism of jet formation were published

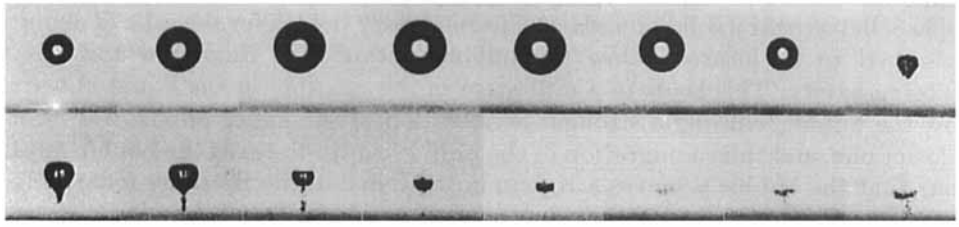

(*a*) $\gamma = 2.30, \epsilon = 1.04, R_{max} = 2.0$ mm

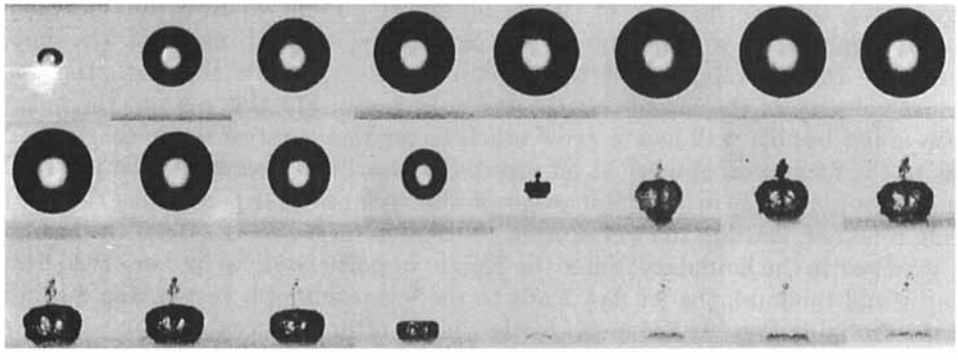

(*b*) $\gamma = 1.56, \epsilon = 1.13, R_{max} = 3.2$ mm

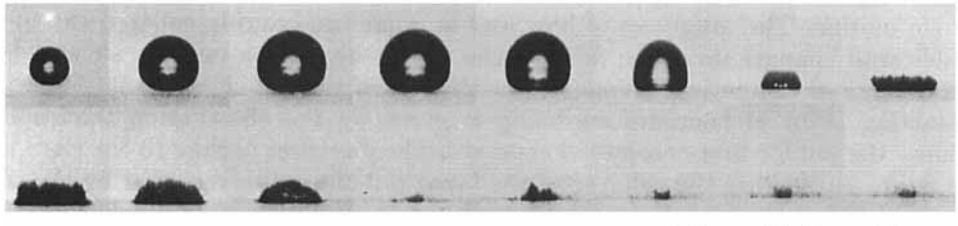

(*c*) $\gamma = 0.75, \epsilon = 1.41, R_{max} = 1.6$ mm

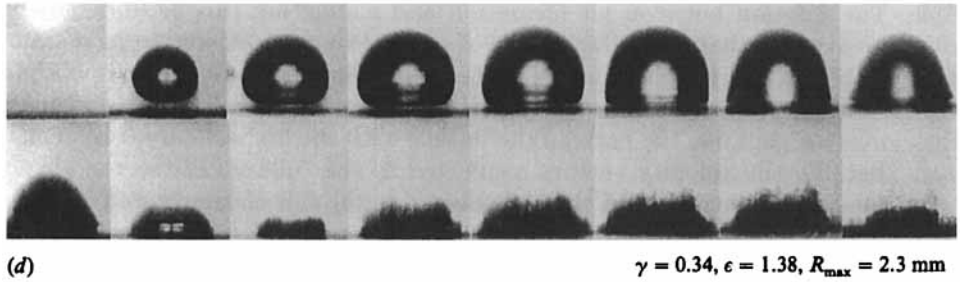

(*d*) $\gamma = 0.34, \epsilon = 1.38, R_{max} = 2.3$ mm

FIGURE 7. Jet formation at different dimensionless distances γ between the site of bubble generation and boundary. R_{max} is the maximum bubble radius and ϵ is the bubble elongation before collapse (see text). The series were taken with the set-up shown in figure 1 at 20000 frames/s. The boundary is given by the darker part below the bubbles in the individual frames. The scale can be read from the maximum bubble radius noted.

as early as 1966 by Benjamin & Ellis. In the following their ideas are applied to bubble collapse near a solid boundary. The boundary (which for the sake of definition is assumed to be located below the bubble) retards the fluid flow towards the collapsing cavity. This leads to a difference in the pressure in the liquid above and below the bubble, causing a stronger acceleration of the upper bubble wall than of the lower one, and thus a migration of the bubble centre towards the boundary. This means that the bubble achieves a Kelvin impulse due to the Bjerknes force which is created by the pressure gradient normal to the boundary. The Kelvin impulse can be regarded as linear momentum of 'the bubble' if a virtual mass induced by the fluid motion is attributed to the cavity. The Bjerknes force almost vanishes in the final stage of the collapse because of the reduction of bubble volume, and the Kelvin impulse approaches a constant value. Since the induced mass of the bubble diminishes during collapse and the Kelvin impulse remains constant, the translational velocity of the bubble centre has to increase. For this reason, the velocity of the upper bubble wall has to grow much faster than that of the lower wall. This leads to the formation of a liquid jet directed toward the boundary. The jet hits the opposite bubble wall in the final stage of the collapse and penetrates the bubble during rebound, causing the well-known protrusion on its lower side, if the bubble is not attached to the boundary. Since the Kelvin impulse needs to be conserved during collapse and rebound, the jet flow leads to the formation of a vortex ring migrating toward the boundary. It becomes clearly visible after the decay of the protrusion.

Lauterborn (1982) has already pointed out that the argument using the Kelvin impulse cannot describe the deformation of the bubble surface in detail, because the Kelvin impulse is an integral value and can only determine aspects of the gross bubble motion. The questions of how and at what time during collapse the upper bubble wall changes its shape to form the tip of the jet can only be answered by experiments or theoretical investigations that track the bubble dynamics in detail. A starting point of heuristic reasoning is given by the observation that during collapse the bubble first becomes elongated in the direction normal to the rigid wall (see figure 7), because the collapse of the lower bubble wall is retarded by the solid boundary. The extent of the elongation ϵ depends mainly on γ. It is defined by $\epsilon = h/R_{\mathrm{hor}}$, where R_{hor} denotes the horizontal bubble radius at the instant of maximum bubble elongation, and h is the distance between the level of R_{hor} and the top of the bubble. The relation between jet formation and elongation can be understood by taking into account that the collapse time of a bubble is proportional to its maximum radius. Therefore, more highly curved parts of an elongated bubble corresponding to a smaller bubble radius collapse faster than less curved parts. The top and bottom of the elongated part, i.e. the parts of the bubble with the highest curvature, collapse faster. Thereby, the velocity vectors connected to the collapse of the top elements become much more focused than those connected to the side elements, and the jet and – under certain circumstances – a counterjet are formed (see Lauterborn 1982). Since this process starts earlier when the bubble is more elongated and since the elongation increases with decreasing γ, the jet is developed earlier with lower γ. At large γ, the bottom flow is not inhibited by the wall and an elongation does not develop, i.e. the collapse is spherical. A counterjet (see figure 7*b*) can appear at moderate γ-values, but only for $\gamma > 1$ when the lower bubble wall is not attached to the boundary and features a high curvature. The counterjet is always weaker than the jet owing to the inhibition of the collapse of the bottom flow by the solid boundary.

At bubble collapse, potential energy of the expanded cavity is converted into kinetic energy of the liquid around the collapsing bubble. The driving force for that

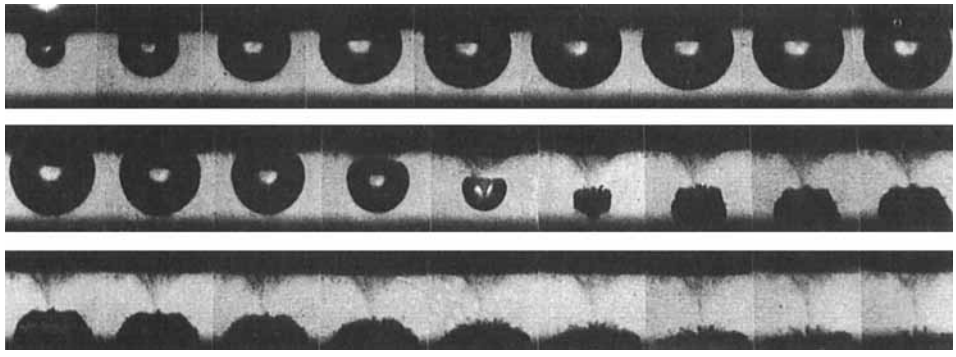

FIGURE 8. Visualization of the jet flow into a cavitation bubble collapsing near a solid boundary. The picture series is taken with the arrangement of figure 1 at 20000 frames/s, $\gamma = 1.25$, $R_{max} = 4.5$ mm. The upper dark band in each frame is a coloured layer of silicone oil on water (brighter background). The solid boundary is visible as the dark stripe in the lower part of each frame.

is the difference between the pressure in the liquid and the pressure in the bubble. As a result of the continuous reduction of the volume available for the fluid inflow, however, the bubble wall is still accelerated for some time in a collapse stage when the pressure in the bubble already exceeds the static pressure in the liquid. This 'geometrical effect' relies on the inertia of the fluid flow and is most pronounced at the upper side of the cavity where the bubble wall has already achieved the highest velocity in the early stages of jet formation. Thus, the jet flow essentially derives its force in the same way as the spherical collapse: it is the concentration of a finite amount of energy into a very small volume. This process can be nicely observed in figure 8, where the jet flow has been made visible by stratifying a coloured layer of silicone oil with the viscosity of water above a 7.5 mm thick water layer covering a solid boundary. In this arrangement, the jet develops earlier than after bubble generation in pure water, because the density of silicon oil ($\rho = 0.773$ g/cm^3) is much lower than the density of water, so that the effect of the interface between both liquids resembles that of a free surface (see Blake & Gibson 1981).

Figure 9 shows the results of the evaluation of a photographic series taken with time-resolved particle image velocimetry at a framing rate of 10 kHz. As expected, the largest flow velocities are found on the side of the bubble where the jet is developing toward the solid boundary. Jet formation is further indicated by the fact that at the end of the collapse the velocity vectors do not point toward the centre of the bubble, but toward a spot close to its surface on the side opposite to the solid boundary (see also figure 10*b*). The fluid flow is thereby focused and strongly accelerated. Figure 9(*g*) shows that during the second collapse a vortex ring is formed as a consequence of jet flow through the bubble.

As indicated by figure 9, no satisfactory temporal resolution of the velocity field evolution in the vicinity of the bubble could be achieved even with the highest possible framing rate of 10 kHz. In addition, the spatial resolution could not be made to exceed 1.5 data points per mm^2 because of the small size of the photographic negative which had to be used due to the high framing rate. Therefore, a different approach was attempted to increase spatial resolution. The image quality was improved by using a framing rate of 5 kHz and a larger image scale. The velocity field dynamics was now followed by taking pictures of different series photographed at different stages of the bubble collapse. Figure 10 contains two velocity field

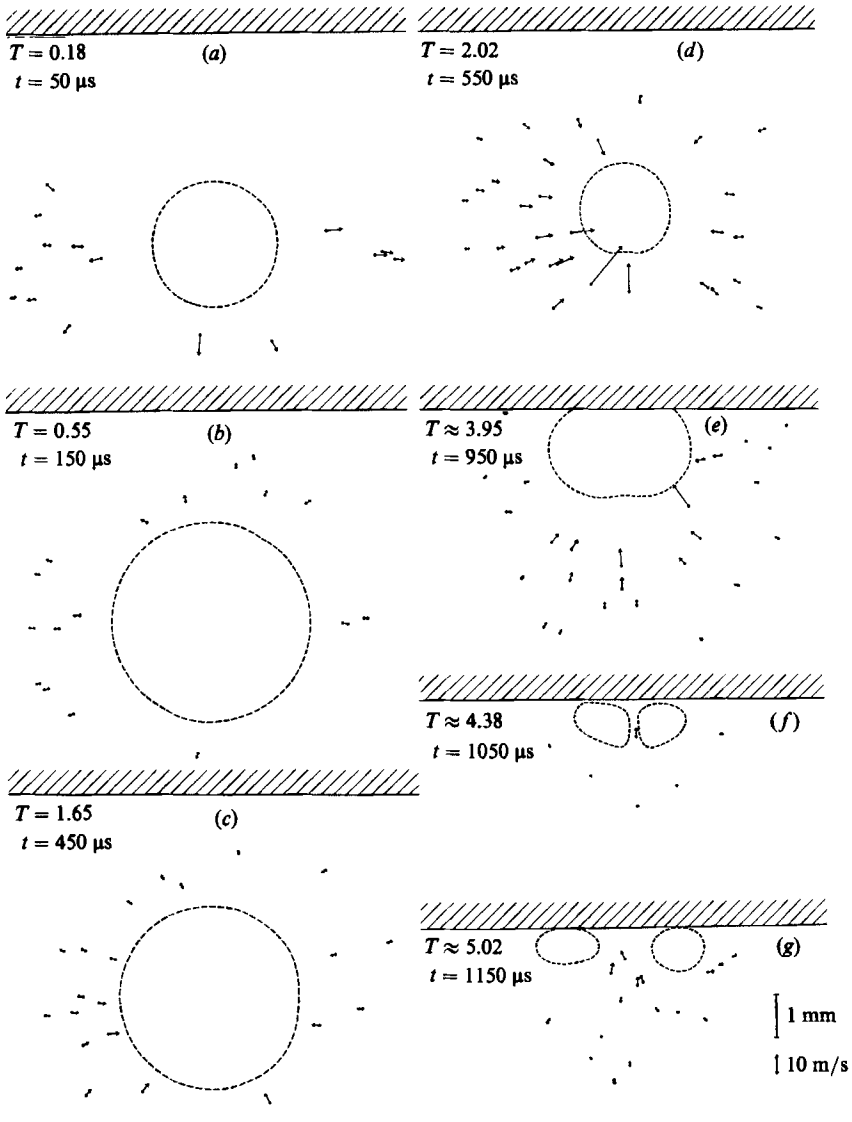

FIGURE 9. Evolution of the velocity field around a laser-generated cavitation bubble close to a solid boundary (hatched area). The first collapse occurs shortly after (*d*), the second collapse shortly after (*e*). $\gamma = 1.9$, $R_{max} = 2.5$ mm. Time t is normalized by Rayleigh's collapse time T_c of a spherical bubble: $T = t/T_c$, with $T = 0$ corresponding to the instant of bubble generation and $T = 2.0$ corresponding to the instant of spherical collapse. The length of the arrows represents the fluid velocity at their respective starting point. Figure adapted from Vogel & Lauterborn (1988*a*).

representations for $\gamma = 2.4$ achieved by this procedure. In this case, spatial resolution is two to three data points per mm^2. The dynamic range of the velocity measurement is about 15:1.

Interpolation of the velocity fields in figure 10 results in the pathline portrait in figure 11 (*a*). Here, the solid boundary is drawn at the bottom of the diagram in order to facilitate comparison with the numerical results in figure 11 (*b*). The pathlines up to bubble shape 1 were obtained from figure 10 (*a*). Figure 10 (*b*) allowed their continuation up to shape 2. The pathlines within shape 2 are speculative

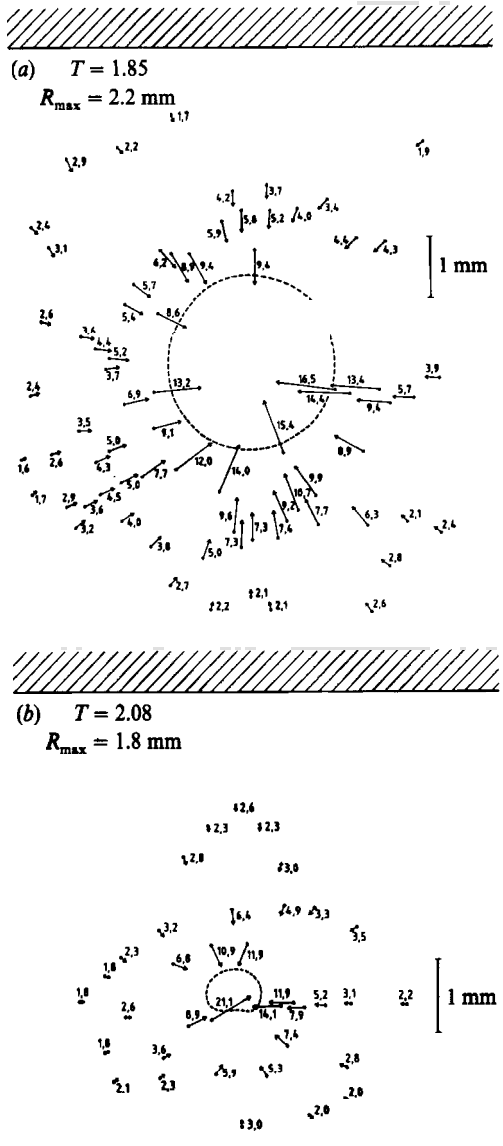

FIGURE 10. Velocity field in the vicinity of a cavitation bubble collapsing near a solid wall (hatched area at the top) at times (*a*) $T = 1.85$ and (*b*) $T = 2.08$, $\gamma = 2.4$. The velocity values are given in m/s. The diagrams are taken from two different series. Figure adapted from Vogel & Lauterborn (1988*a*).

continuations of the flow pattern in the bubble vicinity. Figure 11 (*a*) gives a good visualization of the fluid flow concentration during bubble collapse which results in jet formation. For a comparison of the experimental results with theory, in figure 11 (*b*) a pathline portrait for several points on the bubble surface is shown which was numerically calculated by Kucera & Blake (1988) using the boundary integral-method developed by Blake *et al.* (1986). There is remarkably good agreement between experiment and theory.

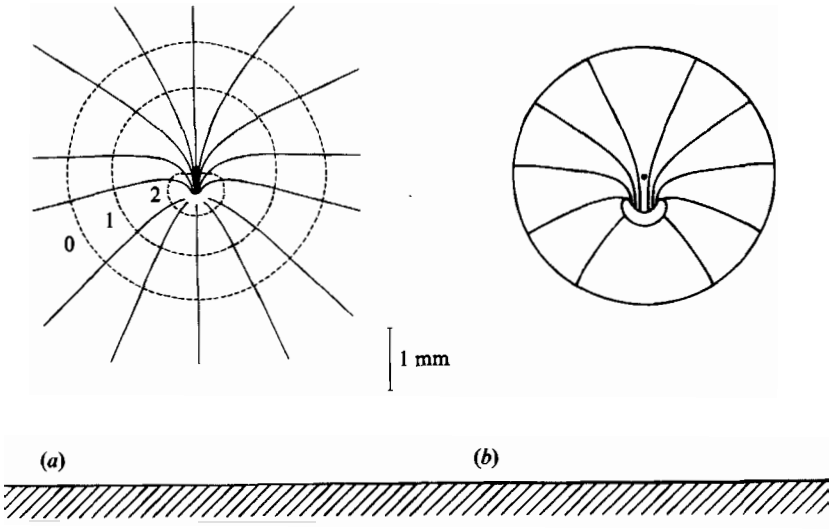

FIGURE 11. (*a*) Experimentally obtained pathline portrait of the flow around a collapsing cavitation bubble near a solid wall at $\gamma = 2.4$. Bubble shape 0 represents the bubble at maximum expansion, shape 1 corresponds to $T = 1.85$ and shape 2 to $T = 2.08$. (*b*) Calculated pathline portrait for $\gamma = 2.4$ from Kucera & Blake (1988) for several points on the wall of the collapsing bubble. The dots in (*a*) and (*b*) indicate the location of bubble formation. Figure adapted from Vogel & Lauterborn (1988*a*).

3.2. *Ring vortex dynamics*

Figures 12 and 13 show in side view and top view the bubble dynamics for relatively large distances between bubble and boundary ($\gamma = 2.55$ in figure 12*a* and $\gamma = 2.15$ in figure 13*a*). A ring vortex is formed after the first collapse, the core of which is the cavitation bubble. The ring vortex which conserves the Kelvin impulse of the cavity becomes clearly visible only after the decay of the bubble protrusion preceding the second collapse. After taking a toroidal shape, the bubble distintegrates into various parts which collapse separately but nearly at the same time and coalesce again during rebound. The ring vortex persists during several oscillations of its toroidal bubble core (figure 12). It migrates toward the solid boundary and starts to expand as soon as it reaches the boundary (figure 13). After the second collapse, the vortex core takes a polygonal shape which probably can be attributed to instability waves on the vortex. This phenomenon has also been observed by Maxworthy (1977) on turbulent vortex rings in single-phase flows. The jet is visible in the bubble centre as a dark bar in side view and as a dark spot in top view. The migration of the bubble or ring vortex, respectively, is shown in figure 14 for the picture series from figures 12(*a*) and 13(*a*). During first and second bubble collapse, the migration is accelerated, which reflects the conservation of the Kelvin impulse as described in §3.1. The Kelvin impulse is then carried by the ring vortex moving with nearly constant velocity towards the boundary. The mean velocity is 6.4 m/s for the vortex in figure 12(*a*) and 5.2 m/s in figure 13(*a*). The smaller velocity in the second case results from the smaller size of the bubble involved.

Figure 15 contains some pictures taken immediately after first bubble collapse with the apparatus depicted in figure 2. In each picture the shock wave emitted during bubble rebound is visible as a bright ring surrounding the bubble. In the lower right picture one can see two shock waves indicating an irregular bubble collapse due to deviations from sphericity of the expanded bubble. The images of the shock waves

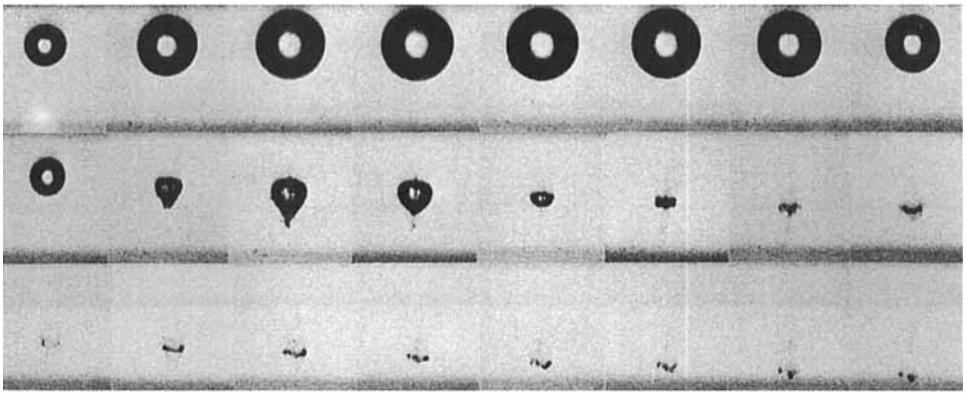

(*a*)

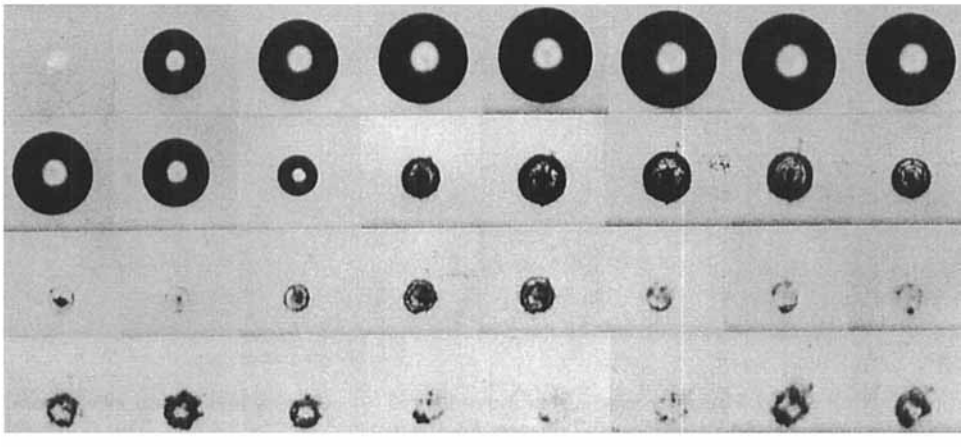

(*b*)

FIGURE 12. Ring vortex formation near a solid boundary (*a*) in side view according to figure 1 (*b*), and (*b*) in top view with line of sight as in figure figure 1 (*c*). Picture series taken at 20000 frames/s. (*a*) $\gamma = 2.55$ and $R_{max} = 2.5$ mm, (*b*) $\gamma = 2.3$ and $R_{max} = 2.1$ mm. In (*a*) the solid boundary is visible as a dark stripe in the lower part of each frame. In (*b*) the boundary is parallel to the plane of the paper and transparent for photographic reasons. Here the dark lines at the lower and upper border of some frames are the actual picture edges.

are blurred because of the relatively long exposure time of about 1 μs. The vertical bar through the shock-wave image in the left picture is due to the directional sensitivity of the high-pass filtering with a vertical wire. It can be inferred from the photographs that the lower bubble wall opposite to the jet is not pierced by the jet during collapse but pushed ahead during rebound. Otherwise the jet flow would have been visible as a bright bar below the bubble because of the sensitive spatial filtering technique applied. The temperature gradient of 1 K/mm around the site of optical breakdown leads to a difference of several K between the temperature of the liquid close to the upper and lower wall of the expanded bubble. This is because during expansion the liquid volume surrounding the laser focus is distributed into a thin layer around the bubble without affecting the temperature distribution slightly further away. The visualization of the jet flow in figure 8 shows that during jet formation liquid that had been more than 1 mm away from the upper bubble wall is

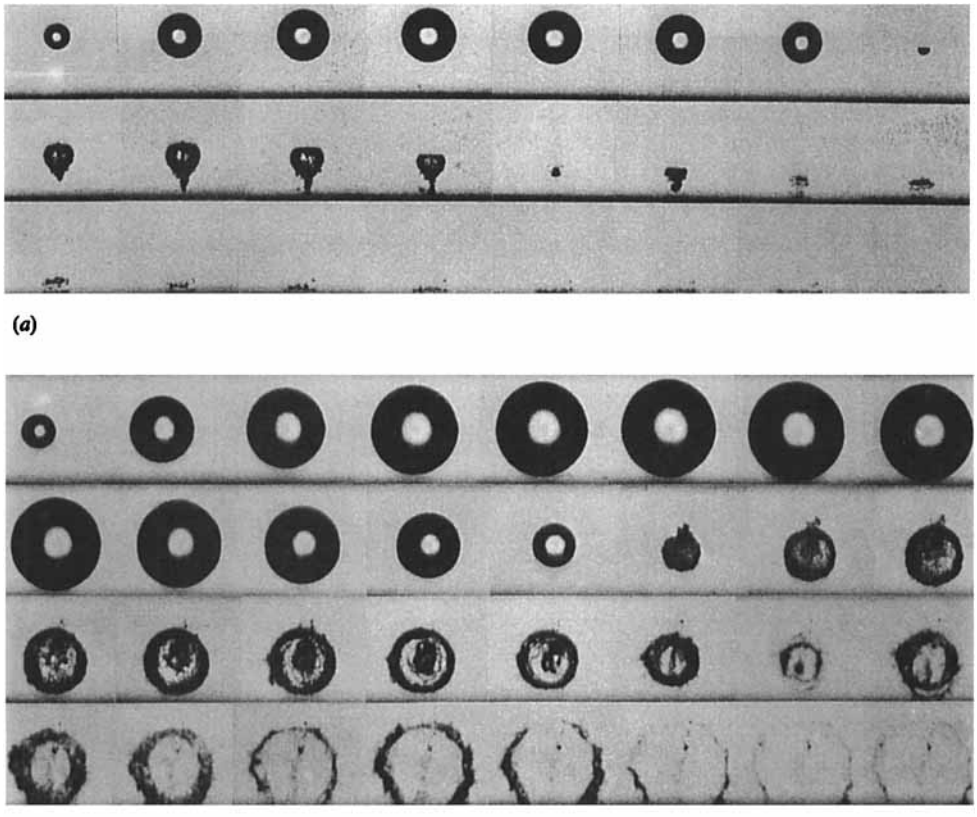

(a)

(b)

FIGURE 13. Ring vortex formation near a solid boundary in (*a*) side view and (*b*) top view. Framing rate 20000 s^{-1}. (*a*) $\gamma = 2.15$ and $R_{max} = 2.05$ mm, (*b*) $\gamma = 1.9$ and $R_{max} = 2.6$ mm. The explanation of the dark borders of the frames is as given for (*a*) and (*b*) in figure 12.

entrained into the bubble. The temperature of this liquid certainly differs from that of the liquid below the bubble by several K – much more than the temperature difference of 0.5 K necessary for detecting the jet (see §2.1).

The bubble content of vapour and gas possibly acts as a cushion which in conjunction with the surface-tension forces maintains the liquid surfaces of jet tip and bubble wall intact. This prevents the penetration of the lower bubble wall immediately after impingement of the jet. In fact, the jet is observable as a bubble protrusion in normal photography only owing to this gas and vapour layer surrounding it. This means on the one hand that the tip of the jet can be identified with the tip of the bubble protrusion, and on the other hand that, although the vorticity has already built up in the course of the first collapse (see figure 11*a*), the vortex ring develops only after the disintegration of the protrusion shortly before the second collapse. This process is visible in figure 7(*a*) and shown with high temporal resolution in figure 16. Induced by the ring vortex in the liquid surrounding the cavity, there is probably another vortex generated inside the bubble which becomes stronger during collapse owing to the reduction of bubble volume and compression of its content. If the ring vortex inside the bubble behaves similarly to turbulent ring vortices in single-phase flows, a wake is formed upstream behind the ring (Maxworthy 1974). This may be the cause of the deformation of the upper bubble side, the

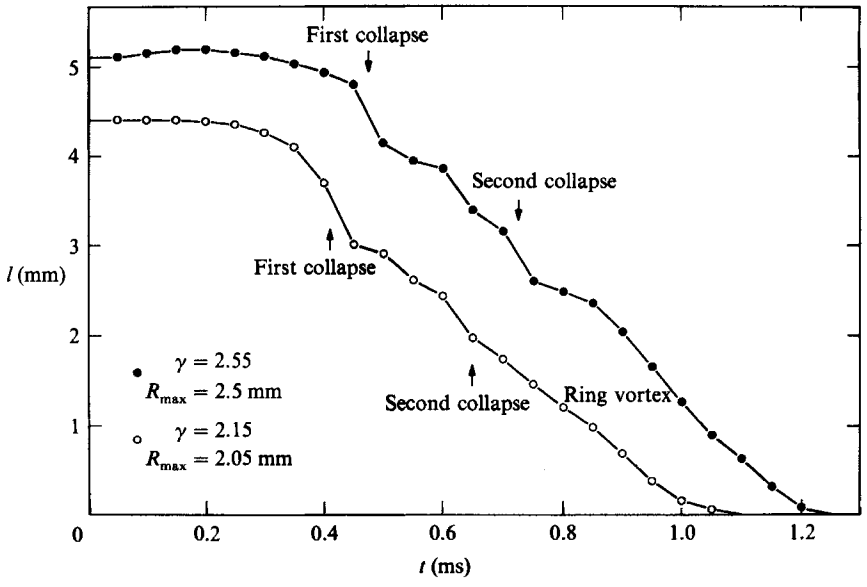

FIGURE 14. Development of distance l between bubble centre and boundary in the photographic series of figures 12(*a*) and 13(*a*).

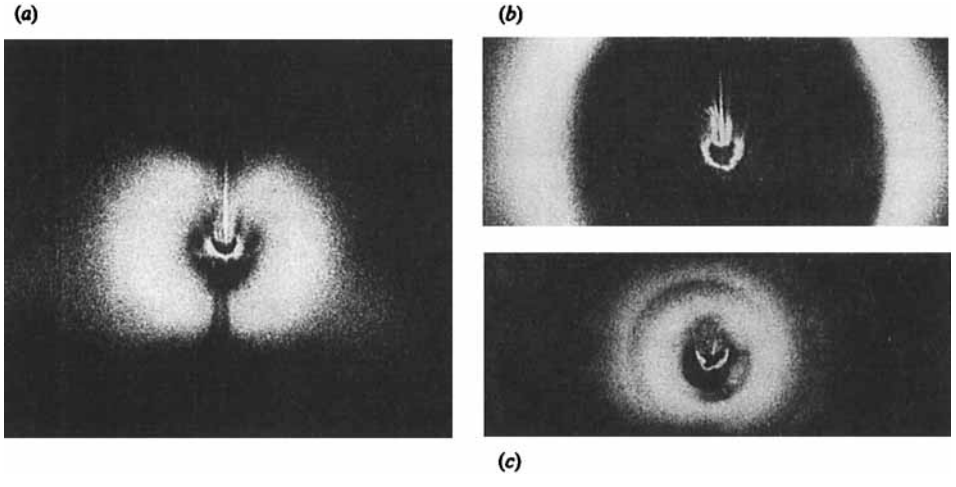

FIGURE 15. Schlieren pictures taken immediately (i.e. 1–3 μs) after the first collapse of three cavitation bubbles with $\gamma = 2.2$ and (*a*) $R_{max} = 1.5$ mm, (*b*) $R_{max} = 1.6$ mm, (*c*) $R_{max} = 2.5$ mm. The solid boundary is below the bubbles outside the frame format. The frame sizes are (*a*) 6 mm × 6.8 mm, (*b*) 4 mm × 10 mm and (*c*) 6.5 mm × 16 mm.

development of which can be observed while the jet keeps flowing through the bubble. This interesting feature is not an exception but is almost typical for γ-values higher than 2 when no or only a weak counterjet appears during first collapse.

With decreasing γ some changes are observed in the scenario described above. In figure 17, where γ is 1.66, the bubble touches the boundary during rebound after first collapse so that a ring vortex can only exist for a very short period during second collapse when the lower bubble side is again detached from the boundary (third and fourth frame). In the fourth frame instability waves can be seen on the toroidal

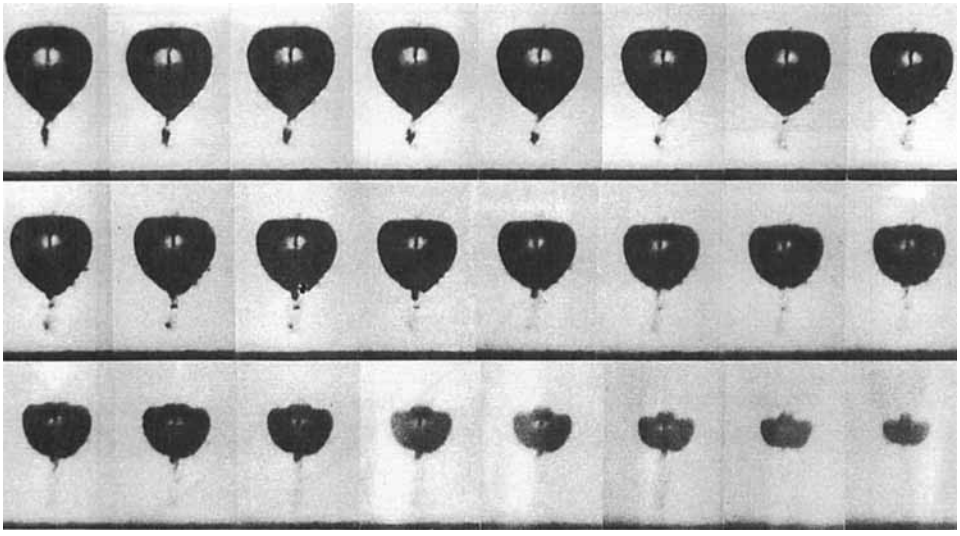

FIGURE 16. Development of a ring vortex and formation of a wake during second bubble collapse. Series taken with the rotating mirror camera at a framing rate of 300000 s^{-1}, $\gamma > 2$. The solid boundary is visible as the dark stripe at the lower edge of each frame. Frame size 4.5 mm × 3 mm.

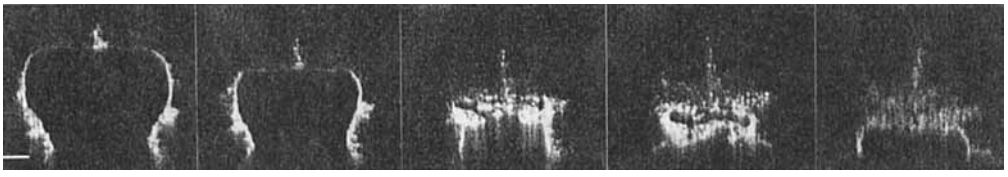

FIGURE 17. Second bubble collapse at $\gamma = 1.66$ and $R_{max} = 3.3$ mm. Series taken with spatial filtering at 20000 frames/s. The location of the solid boundary is indicated by the white horizontal bar in the left frame. Frame size 4.5 mm × 5 mm.

cavity. They are visible with the schlieren technique because it allows one to distinguish between the principal cavity which blocks out the light and the cloud of microbubbles surrounding the cavity which appear bright owing to their high scattering efficiency. The microbubbles generally arise during the first bubble collapse, since deviations from sphericity of the expanded bubble lead to instabilities growing during collapse which finally cause the separation of parts of the principal bubble (see Strube 1971). Figure 18 shows the first and second collapse for $\gamma = 1.37$. After the first collapse, no ring vortex forms but merely a radial outward flow on the solid boundary arises from the jet decelerating the second collapse in horizontal direction. Apparently, the toroidal bubble disintegrates into several separately collapsing parts. This is gathered from the observation of two acoustic transients in frame 15 emitted from different sites during second collapse (the acoustic transient at the left side of the picture is weak and only faintly visible). The protrusion of the upper bubble side, which shortly after formation appears as a cloud of microbubbles, indicates that a counterjet is formed during first collapse (see §3.3 below).

The bubble dynamics is especially interesting when γ is at about unity. In this case, a ring vortex has already formed *before* the first collapse. Figure 19 shows a bubble with $\gamma = 0.96$ at the stage of maximum expansion, at an intermediate stage and about 30 μs before collapse. In the last picture, the upper bubble side has already

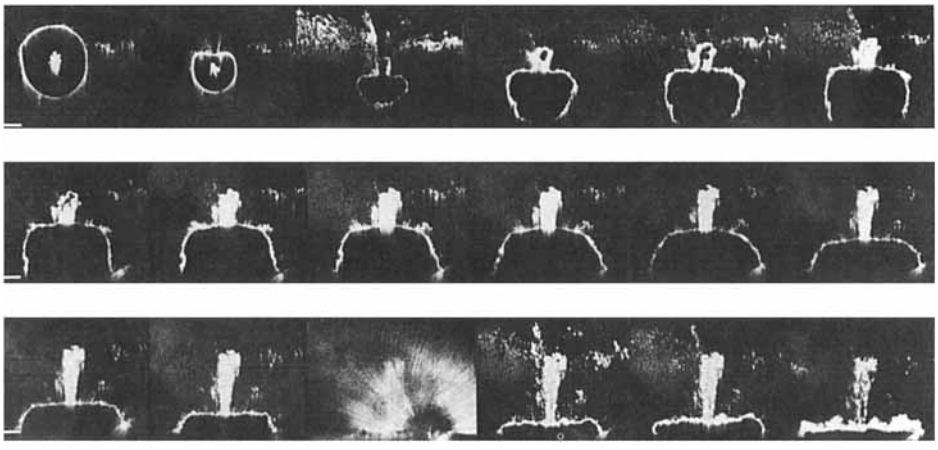

FIGURE 18. First and second bubble collapse at $\gamma = 1.37$ and $R_{max} = 4.0$ mm. Series taken with spatial filtering at 20000 frames/s. The boundary is indicated by the white bar in the left frames. Frame size 4.8 mm × 5.6 mm.

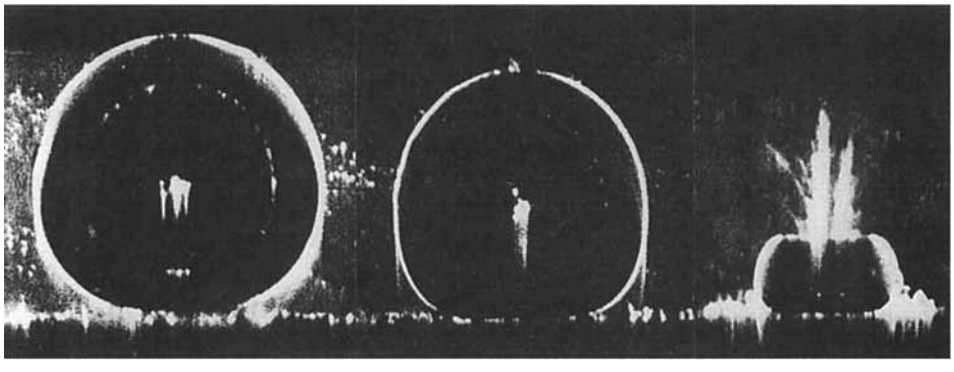

FIGURE 19. Schlieren pictures of bubble collapse at $\gamma = 0.96$ and $R_{max} = 3.9$ mm. The left picture shows the stage of maximum expansion ($T = 1.03$), the middle frame was taken at $T = 1.80$ and the right picture at $T = 2.19$, corresponding to an instant about 30 μs before collapse. The location of the solid boundary is given by the white dotted line of microbubbles below the laser-produced cavitation bubble. Height of the frames 5 mm.

involuted to form the tip of the jet and the lower bubble side has detached from the rigid boundary. The jet touches the opposite bubble wall before the bubble reaches its minimum size and most probably pierces the wall because it does not give way to the jet as in the case of large γ, where the collision between jet and bubble wall coincides with the beginning of the rebound. Thus, a ring vortex develops and during the final stage of the collapse the bubble has a toroidal form as already observed by Shutler & Mesler (1965).

The first numerical investigation of the aspherical collapse at $\gamma = 1.0$ was done by Plesset & Chapman (1971). Their work has set a historical milestone which was only surpassed 15 years later by Blake *et al.* (1986). In figure 20, the results from both papers are compared at different times $T = t/T_C$ with the experimental data from figure 19. Here T_C is Rayleigh's collapse time, and t starts with the instant of bubble generation. In order to facilitate the comparison, the elongation ϵ of the upper part of the bubble and the ratio $\beta = R_v/R_{hor}$ of vertical and horizontal bubble radius is

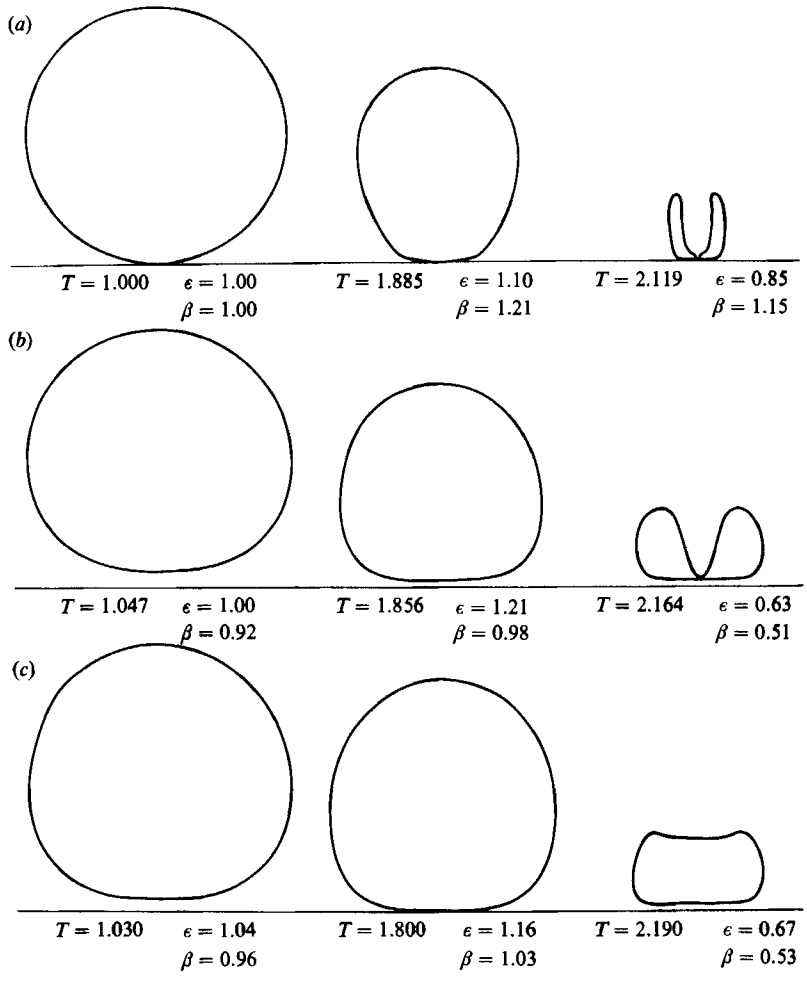

FIGURE 20. Comparison of numerically calculated bubble shapes taken (*a*) from Plesset & Chapman (1971) and (*b*) from Blake *et al.* (1986) with experimentally determined curves (*c*) obtained from the picture series in figure 19. $\gamma = 1.0$ in the numerical calculations, and $\gamma = 0.96$ in the experiment. T, ϵ and β are explained in the text. Note that (*a*) and (*b*) show a cross-section of the bubble, whereas in (*c*) the bubble shape is depicted in side view.

given for each diagram. The comparison reveals that the results from the model of Blake *et al.* (1986) agree better with the actual bubble dynamics than those of Plesset & Chapman (1971). This is very reasonable, because Plesset & Chapman only considered the collapse phase from a sphere, whereas Blake *et al.* also included the growth phase.

In the parameter range around $\gamma = 1.0$, the fluid motion directed radially towards the bubble centre is partly transformed into the rotational movement of the ring vortex. The consequence is, as discussed in a theoretical paper by Chahine & Genoux (1983), that the bubble implosion is decelerated and the bubble remains relatively large during collapse. In figure 21, the collapse is compared for the cases of $\gamma = 2.2$ and $\gamma = 0.96$. The minimum extension of the bubble is 3 mm horizontally and 1 mm vertically at $\gamma = 0.96$ but only 0.6 mm horizontally and about 80 μm vertically at $\gamma = 2.2$. Therefore, the pressure rise inside the bubble is relatively low at $\gamma = 0.96$ resulting in a weak sound emission, as will be shown in §3.4.3 below.

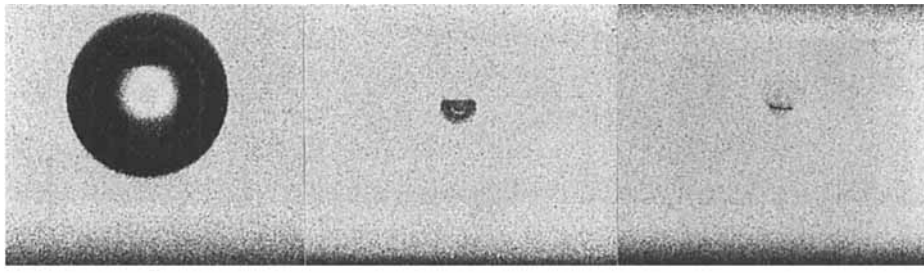

(*a*)

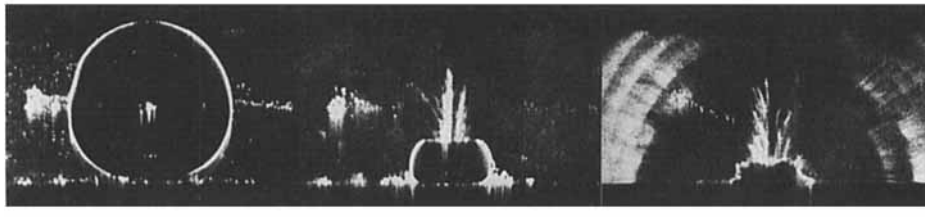

(*b*)

FIGURE 21. Comparison of bubble collapse at different distances from the boundary. (*a*) $\gamma = 2.2$ and $R_{max} = 2.7$ mm, (*b*) $\gamma = 0.96$ and $R_{max} = 3.9$ mm. In each case, the bubble is shown in the stage of maximum expansion in the left frame and at the instant of minimum size in the right frame. In (*a*) the middle frame was taken about 1 μs before collapse and in (*b*) about 30 μs before collapse. The pictures in (*a*) were taken with the apparatus from figure 1 and those in (*b*) with that from figure 2. The solid boundary is given in (*a*) by the dark stripe at the lower edge of each frame, and in (*b*) by the white dotted line of microbubbles below the principal bubble. Height of the frames: (*a*) 4.3 mm and (*b*) 5 mm.

3.3. *Counterjet formation*

In figures 7 (*b*) and 18, a protrusion on the upper bubble side can be seen immediately after the first collapse. This phenomenon has been interpreted by Lauterborn & Bolle (1975) as a consequence of a counterjet, i.e. a jet flowing in the opposite direction to the principal jet. Two typical cases of bubble collapse with and without the development of a counterjet are compared in figure 22. Figure 23 contains a summary of the conditions of counterjet formation which has been obtained by evaluation of high-speed photographic series. It appears that the occurrence of a counterjet is correlated with the distance γ between bubble and boundary as well as with the bubble elongation ϵ. Although the elongation is mainly a function of γ, it can also be affected by the form of the optical breakdown used for bubble generation: an elongated plasma causes a greater elongation of the bubble during the final collapse stage than a spherical plasma. To facilitate the discussion of figure 23, the limits of the parameter ranges with weak, pronounced and strong counterjets are sketched. It is clearly visible that the strength of the counterjet increases with decreasing γ (as long as γ is larger than one) and with increasing ϵ. As pointed out in §3.1, a small γ-value and a large ϵ-value also lead to early jet formation. It can therefore be assumed that the occurrence of a counterjet is related to the instant of jet formation.

The following heuristic explanation of counterjet formation takes up the ideas of jet formation presented in §3.1. Although the driving force for bubble collapse is the difference between the pressure in the surrounding liquid and that inside the bubble, the bubble wall is still accelerated when the pressure inside the bubble exceeds the

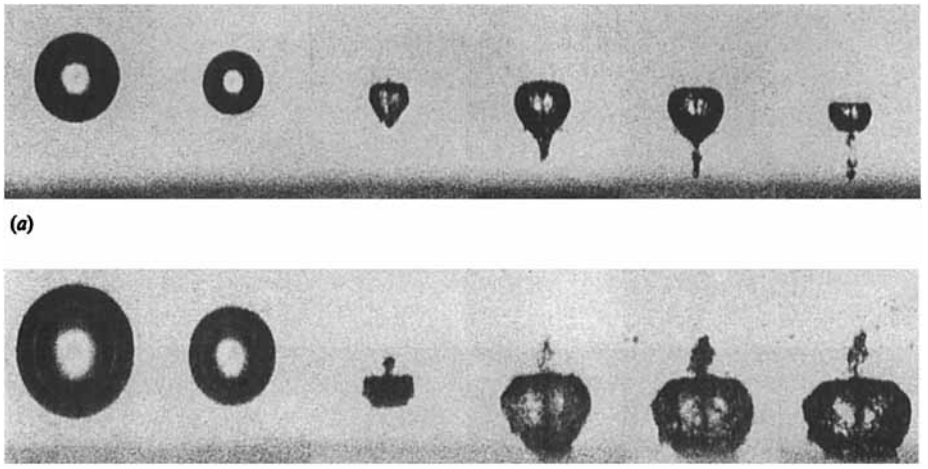

FIGURE 22. First bubble collapse (*a*) without and (*b*) with counterjet formation. (*a*) $\gamma = 2.3$, $R_{max} = 2.0$ mm, $\epsilon = 1.04$; (*b*) $\gamma = 1.56$, $R_{max} = 3.2$ mm, $\epsilon = 1.13$. Pictures taken with the apparatus from figure 1 at 20000 frames/s. The solid boundary is at the lower edge of each frame. Frame size in (*a*) and (*b*) 7.3 mm × 5.6 mm.

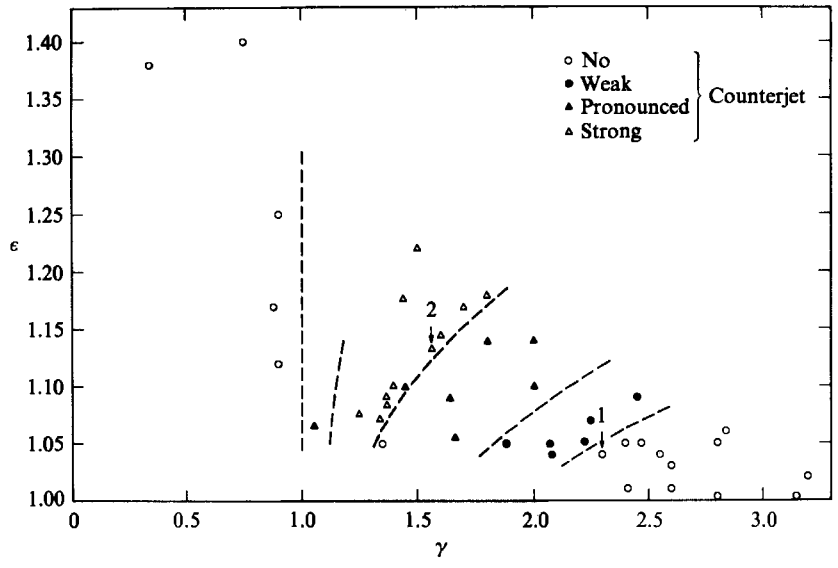

FIGURE 23. Strength of the counterjet as a function of the dimensionless distance γ between bubble and boundary and the bubble elongation ϵ. The measurement points 1 and 2 correspond to the photographic series of figures 22(*a*) and 22(*b*).

static pressure in the liquid, because the fluid flows into a cavity with continuously decreasing volume. Obviously, this acceleration due to inertia forces is effective only as long as the curvature of the bubble wall is concave. Once the convex tip of the jet is formed, its velocity remains fairly constant. This explains why the jet achieves a higher velocity at $\gamma = 1.5$ than at $\gamma = 1.0$ when the tip of the jet appears earlier than in the former case (see Plesset & Chapman 1971; Blake *et al.* 1986). Since the curvature of the lower bubble side is concave during the whole collapse time, it is

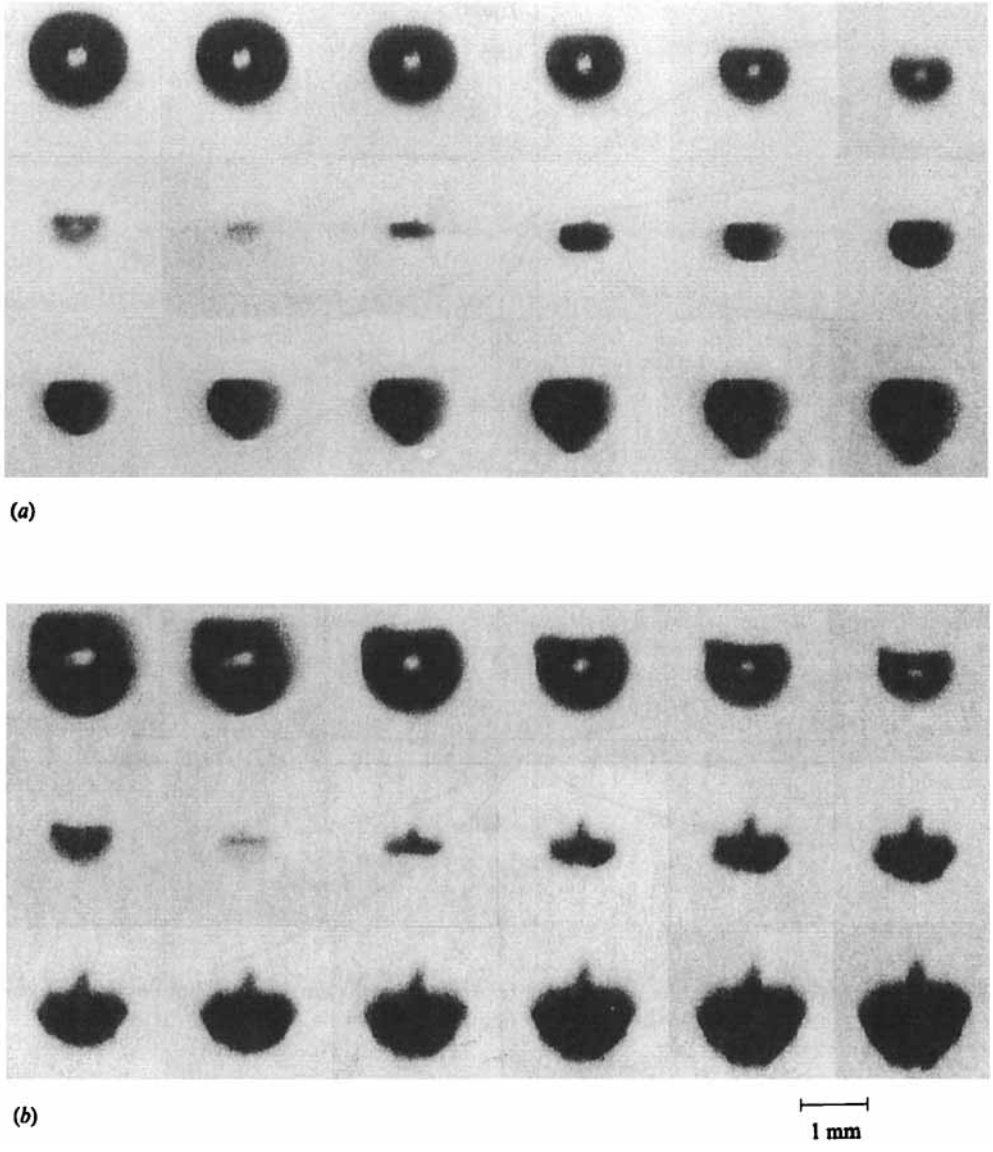

FIGURE 24. Comparison of bubble collapse (*a*) without and with (*b*) counterjet formation. Series taken with the rotating mirror camera at 940000 frames/s in (*a*) and 880000 frames/s in (*b*). The solid boundary is below the bubble outside the frame format. Frame size in (*a*) and (*b*) 3 mm × 2.5 mm.

accelerated until the very end of collapse. Therefore, the velocity of its middle part can exceed the jet velocity when γ is low enough to cause a relatively slow jet. This defines the condition of counterjet formation.

The above considerations are illustrated by figures 24 and 25. Since the photographic record of the bubble dynamics with a rotating mirror camera at very high framing rates can only cover a small part of the collapse process, neither the maximum bubble radius nor γ are known exactly. However, it can be inferred from the diagram in figure 23 that γ must be larger than 2.3 in figure 24 (*a*) and smaller than 2.0 in figure 24 (*b*). Figure 25 shows the movement of the top, bottom and centre

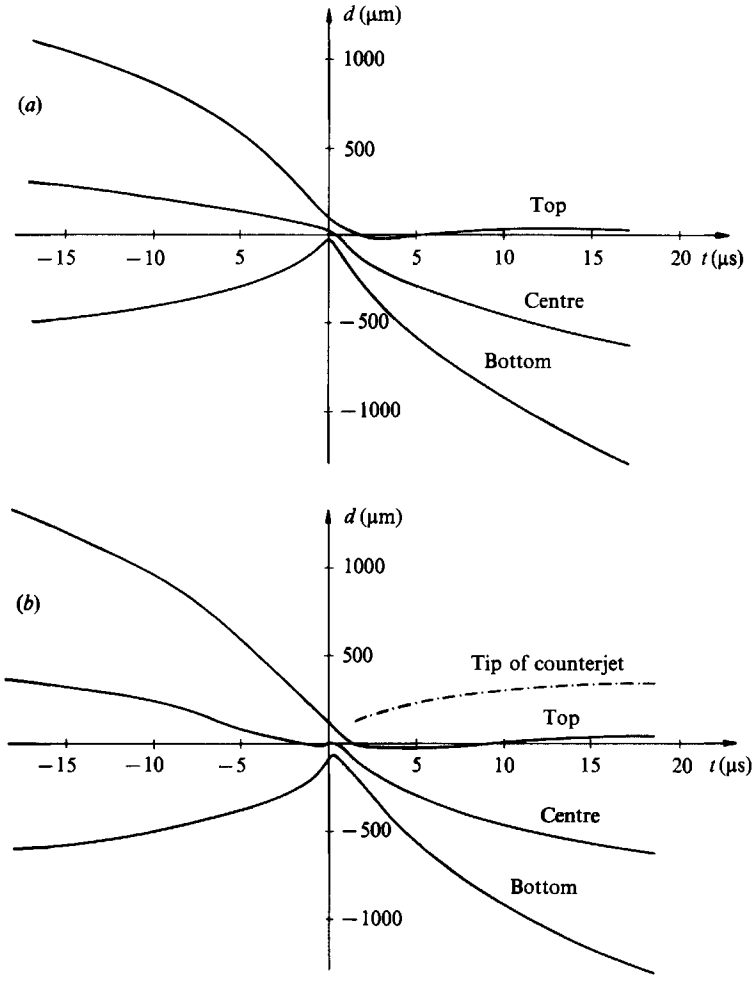

FIGURE 25. Distance d from the collapse centre for different points of the bubble wall versus time. (a) is evaluated from figure 24(a) and (b) from 24(b).

of the bubble and of the tip of the counterjet. The respective velocities and accelerations can be determined from the first and second derivatives of the curves. Figure 24(b) shows that during collapse with counterjet formation the top of the bubble is already involuted 6 μs before collapse, and from figure 25(b) one can see that it is no longer accelerated after this time. The bottom of the bubble, however, is accelerated until the end of collapse so that its final velocity (140 m/s) exceeds that of the upper bubble side (100 m/s). This is the origin of the counterjet which causes a protrusion in the upper bubble wall even before the main jet deforms the lower wall. At the beginning, the upward velocity of the protrusion is 35 m/s, thus being almost as high as the velocity difference between upper and lower wall. After only 10 μs it has decreased to 8 m/s and after 20 μs to almost zero. The diameter of the counterjet is smaller than that of the jet owing to the longer lasting focusing of the fluid flow creating the counterjet. It penetrates the centre of the jet, thereby pushing ahead a part of the compressed gas and vapour inside the bubble by which it becomes visible on the photographs. The protrusion disintegrates into a cloud of microbubbles which remain behind while the bubble centre is migrating

towards the rigid boundary. After a short time, the jet overcomes the distortion by the counterjet due to its larger volume and impulse. However, the jet flow has become extremely turbulent, is thicker than in the case without a counterjet and causes a broader protrusion of the lower bubble wall. The whole surface of the rebounding bubble is rough owing to the interaction between jet and counterjet (see figures 22*b* and 24*b*).

When γ is larger than 2, the mechanism described above is usually not strong enough to cause a counterjet, but it is responsible for the flattening of the bubble during the ultimate collapse phase which can be seen in figure 25(*a*). In this case, the upper bubble wall features no involution until the end of collapse, and its velocity (110 m/s) remains higher than that of the lower wall (90 m/s). When γ is smaller than unity, no counterjet can be developed in spite of early jet formation, because the bottom of the bubble is retained by the solid boundary after the bubble has reached the stage of maximum expansion.

The experiments reveal that at $\gamma = 1.5$ a counterjet is always formed. It is remarkable that this phenomenon does not emerge in any of the numerical calculations performed with this γ-value published to date. Lauterborn & Bolle (1975) compared experimentally determined bubble shapes at $\gamma = 1.5$ and $R_{\max} = 2.6$ mm with curves numerically obtained by Plesset & Chapman (1971). The agreement was very good until the end of the investigated period (about 2 μs before collapse), although the experimental bubble developed a strong counterjet visible after collapse. The middle picture in figure 21(*a*) taken about 1 μs before collapse also closely resembles the diagrams of the latest stage in bubble collapse that could be calculated with the models of Plesset & Chapman (1971) and Blake *et al.* (1986) for $\gamma = 1.5$. Hence, the counterjet formation takes place in the ultimate collapse phase which can no longer be modelled by the numerical calculations. This is also confirmed by figure 25(*b*) showing that the velocity of the lower bubble wall exceeds that of the upper wall only during the final microsecond before collapse. In order to reflect the whole diversity of phenomena observed experimentally, including counterjet and ring vortex formation, the numerical calculations ought to be able to track the bubble dynamics after the jet reaches the opposite bubble wall, and they ought to take into account the bubble content of vapour and gas. These are certainly very important during the final collapse stage, as well as surface-tension forces and the effects of compressibility.

3.4. *Sound emission*

3.4.1. *Profile of the acoustic transients*

The acoustic transients emitted after cavitation-bubble generation and after bubble collapse have been investigated with the experimental arrangement outlined in figure 5. Figure 26 shows typical signals from hydrophone 2 together with the corresponding results of the optical detection. The optical measurement reveals that the acoustic transients are much shorter than the rise time of the pressure transducer. For evaluating the optical measurements, first the distortion of the signal resulting from the nonlinearity of the $U(\phi)$-characteristic of the apparatus (see figure 6) is corrected. Then $p(t)/P_{\max}$ is calculated by numerical integration. Two pressure profiles obtained in this way are given in figure 27. The duration τ (width at half-maximum) of the acoustic transients is about 25 ns both after laser-induced plasma formation and after bubble collapse. The same duration was observed for the acoustic pulses after the second bubble collapse. The pressure pulse caused by the expanding plasma features a steep shock front with a rise time of 10 ns. Since this

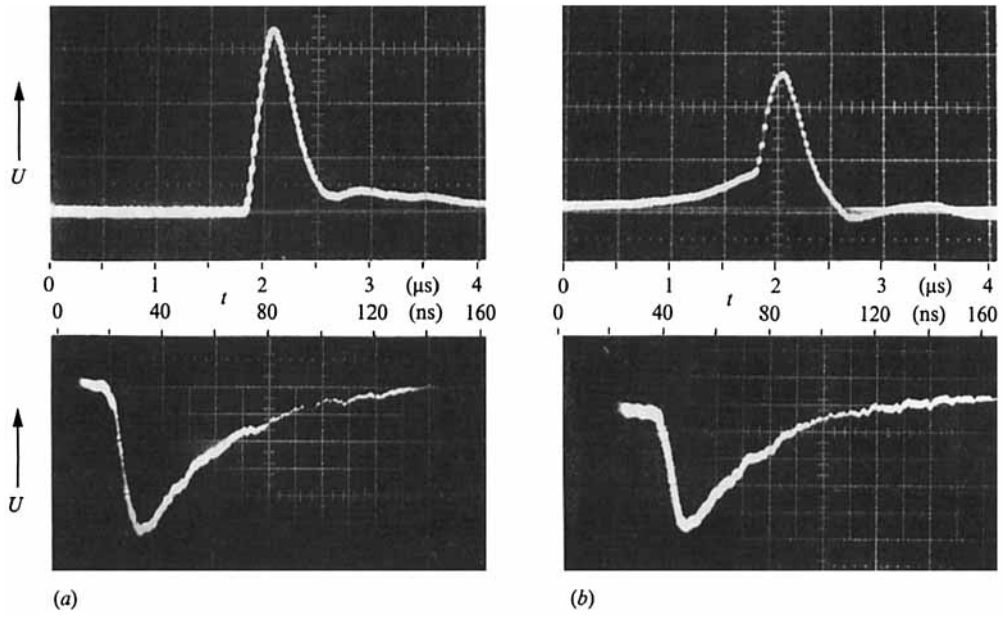

FIGURE 26. Typical signals of the PVDF-transducer (top) and of the photodetector (bottom) (*a*) after laser-induced bubble generation and (*b*) after cavitation bubble collapse. The distance between the emission centre of the acoustic pulses and the probe was 1.2 mm for the optical and 8 mm for the acoustic measurement. Figure adapted from Vogel & Lauterborn (1988*b*).

value equals the temporal resolution of the apparatus, the actual shock front is probably even shorter. During cavitation-bubble collapse, a relatively slow pressure rise occurs within 1–2 μs followed by a shock front similar to that after breakdown. This result can be explained by the theoretical work of Hickling & Plesset (1964) and Fujikawa & Akamatsu (1980). They found a strong pressure rise near the bubble wall during the last stages of the collapse and the evolution of a shock front during the rebound of the bubble. Behind the shock front, the pressure decreases nearly exponentially.

The duration of the acoustic transients was measured as a function of their distance r from the emission centre in the range from 0.6 mm to 6.0 mm. The pulse duration was found to be nearly constant both for the transients after bubble generation and after bubble collapse. A broadening of the pressure profile predicted by the propagation theory for finite-amplitude waves of Cole (1948) and Esipov & Naugol'nykh (1972) was not observed. This surprising result is probably due to the spherical form of the acoustic waves which leads to a rapid decrease of the pressure amplitude so that the domain of nonlinear sound propagation is limited to a small region around their emission centre.

The duration of the acoustic transients emitted during bubble collapse near a solid boundary is the same as during spherical collapse when $\gamma \leqslant 0.75$ or $\gamma \geqslant 1.05$. In the range $0.75 < \gamma < 1.05$ the acoustic pulses are too weak to be detected with the optical technique. The signals from the pressure transducer, however, often have a duration of several microseconds, i.e. longer than the impulse response of the measuring instrument. It is not clear whether this is due to one long pressure pulse or to a series of short pulses which could not be resolved by the transducer. The latter is suggested by the schlieren image in figure 21 (*b*).

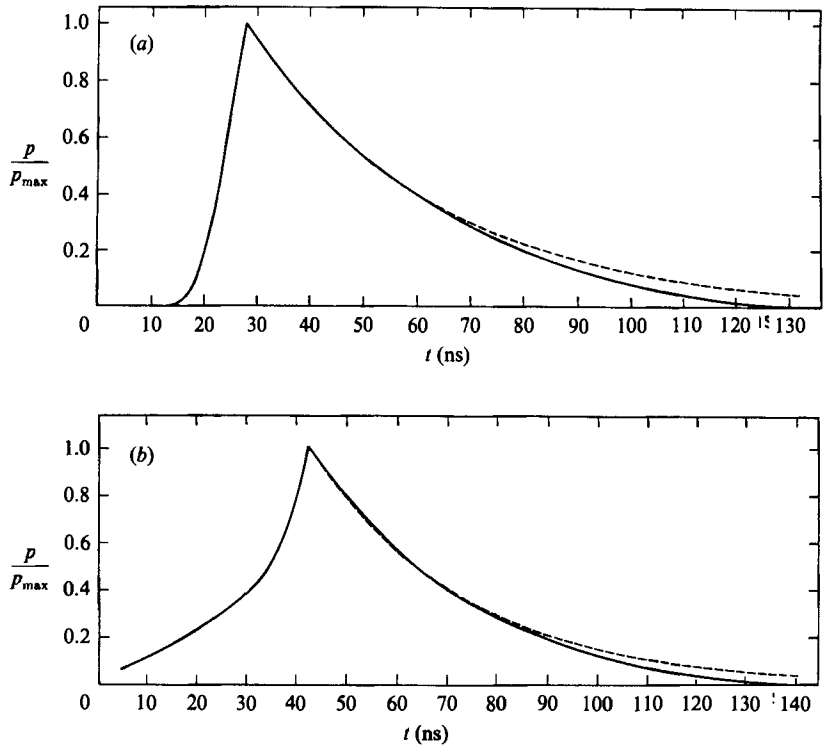

FIGURE 27. Pressure profiles ($p(t)/p_{max}$) of the acoustic transients (*a*) after laser-induced bubble generation and (*b*) after cavitation bubble collapse: ——, experimentally determined profile; ----, exponential decrease. The measurement distance from the emission centre of the acoustic pulses was 1.2 mm. (*a*) and (*b*) correspond to the photodiode signals (*a*) and (*b*) in figure 26. Figure taken from Vogel & Lauterborn (1988*b*).

3.4.2. *Spherical-bubble collapse*

The investigation of the sound emission of spherical cavitation bubbles is of no direct interest for the explanation of cavitation erosion, because bubbles close enough to a solid boundary to cause damage will always collapse aspherically. Nevertheless, it provides the basis for interpretation of the data obtained for the asymmetrical collapse and is to date the only means of comparing experimental results with theory.

The collapse times T_{c1}, T_{c2} and T_{c3} for the first, second, and third spherical bubble collapse are proportional to the maximum bubble radius R_{max} before the respective collapse. The bubble radius can be deduced from the time distance $2T_c$ between the peaks of the pressure signal making use of the relationship

$$R_{max} = \frac{T_c}{0.915\left(\frac{\rho}{p_{stat}-p_v}\right)^{\frac{1}{2}}} \tag{3}$$

derived for spherical collapse by Rayleigh (1917). ρ is the density of the liquid, p_{stat} the static pressure and p_v the vapour pressure of the liquid. The energy E_B of the cavitation bubble is given by

$$E_B = \tfrac{4}{3}\pi (p_{stat}-p_v) R_{stat}^3. \tag{4}$$

The energy loss during bubble collapse is obtained by comparing the different values of the bubble energy before and after collapse. The peak pressure amplitude of the acoustic transients is calculated from the transducer signal, and the pulse duration with the help of (1). In cases where τ could not be determined synchronously with the acoustic measurement, we calculated the peak pressure assuming a pulse duration $\tau = 20$ ns at the site of the transducer. The energy of a spherical acoustic transient as derived by Cole (1948) is

$$E_s = \frac{4\pi r^2}{\rho c} \int p^2 \, dt, \tag{5}$$

where c denotes the sound velocity in the liquid and r the distance between the pressure transducer and the emission centre of the transient.

In figure 28(*a*) the peak pressure of the acoustic transients emitted during the first and second cavitation bubble collapse is plotted versus the maximum bubble radius. The pressure values refer to a distance r of 10 mm between the bubble centre and the site of measurement. The acoustic signals used for evaluation have been selected to exclude as far as possible bubbles that deviate from the spherical form. Those bubbles are indicated by multiple pressure pulses emitted during both bubble generation and collapse, which are easily visible with the optical detection technique. The shock waves measured after the first collapse of a spherical bubble generally have approximately the same amplitude as those emitted by the laser-induced plasma generating the bubble. Figure 28(*b*) shows that the energy of the acoustic transients increases proportionally to the energy of the cavitation bubbles as long as the bubble energy does not exceed 30 mJ, corresponding to a radius of 4 mm. Larger bubbles can only be produced with a high laser pulse energy of more than 300 mJ. Therefore, they probably frequently feature deviations from the spherical form because multiple plasmas are generated in the region surrounding the ruby laser focus. Since these deviations grow during bubble collapse (see Strube 1971; Plesset 1974), the bubble implodes less violently than during spherical collapse and the sound emission is diminished.

The average energy loss of the cavitation bubbles during their first collapse is 84 %. It was found that the major part of it – at most 90 % and on average 73 % – is due to the emission of sound. Heat conduction and viscosity seem to play only a minor part in damping the oscillations of transient spherical bubbles. These findings are in good agreement with the theoretical work reported by Ebeling (1978), Nishiyama & Akaizawa (1979) and Fujikawa & Akamatsu (1980) as well as with the experimental work of Teslenko (1980). The results of Hentschel & Lauterborn (1982), who claimed that only about 1.2% of the bubble energy is converted into acoustic energy, were obtained without properly taking into account the limited bandwidth of the pressure transducer.

In the domain of linear sound propagation – when the pulse broadening and dissipation can be neglected – the amplitude of a spherical acoustic wave is inversely proportional to the distance r. Hickling & Plesset (1964) as well as Fujikawa & Akamatsu (1980) have shown by numerical calculations that the $1/r$ law is also approximately true for the nonlinear domain in the direct vicinity of the collapse centre. In this region, the effects due to the dissipation of sound energy are compensated for by the development of the shock front. As shown in the next paragraph, we found that the minimum radius of laser-produced cavitation bubbles during first collapse is about 50 μm. Taking the experimentally observed pressure amplitudes as a basis and using the $1/r$ law, the pressure at $r = 50$ μm is calculated

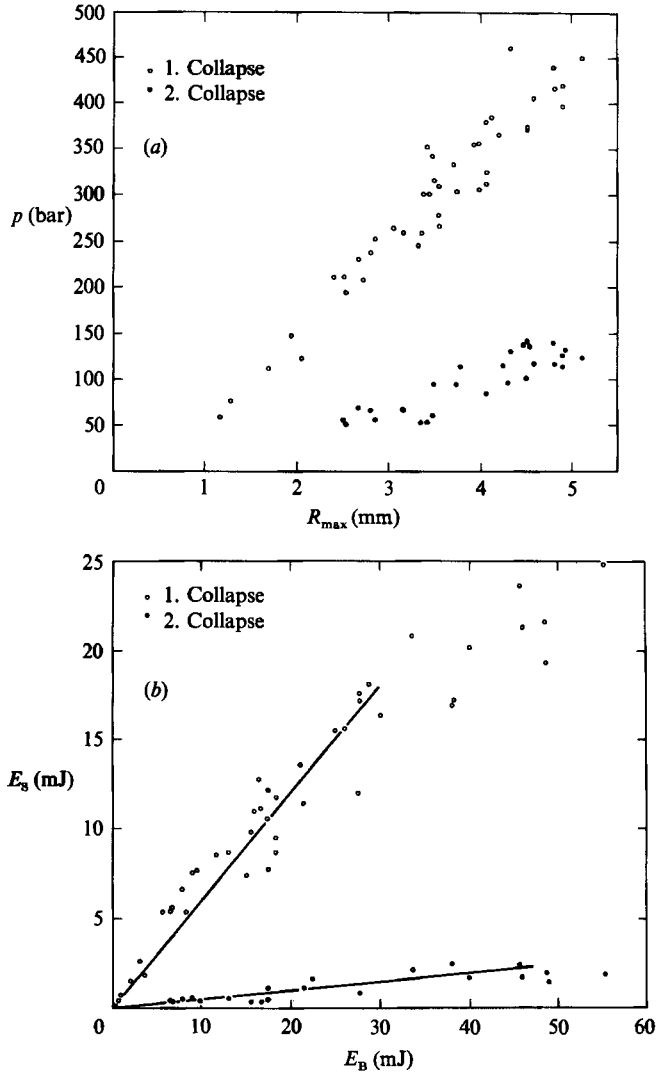

FIGURE 28. (*a*) Peak pressure p of the acoustic transients emitted during first and second spherical bubble collapse as a function of the maximum bubble radius R_{max}. The pressure values are normalized to a distance $r = 10$ mm from the bubble centre. (*b*) Energy E_s of the acoustic transients plotted versus the bubble energy E_B. Figure adapted from Vogel & Lauterborn (1988*b*).

to be 60 kbar when $R_{max} = 3.5$ mm. Thus, the maximum pressure developed inside the bubble during collapse is about 60 kbar.

The minimum bubble radius during spherical collapse was measured with the help of the high-speed photographic series shown in figure 29, which were taken with the image converter camera at 1 million frames/s. For each series, a radius-time curve obtained through numerical calculations based on the model of Gilmore (1952) was fitted to the experimentally determined radius values. The Gilmore model takes into account the effects of compressibility of the liquid, the surface tension and the bubble content of permanent gas. The bubble radius from the first picture was in each case taken as the initial condition for the numerical calculation and the best fit was

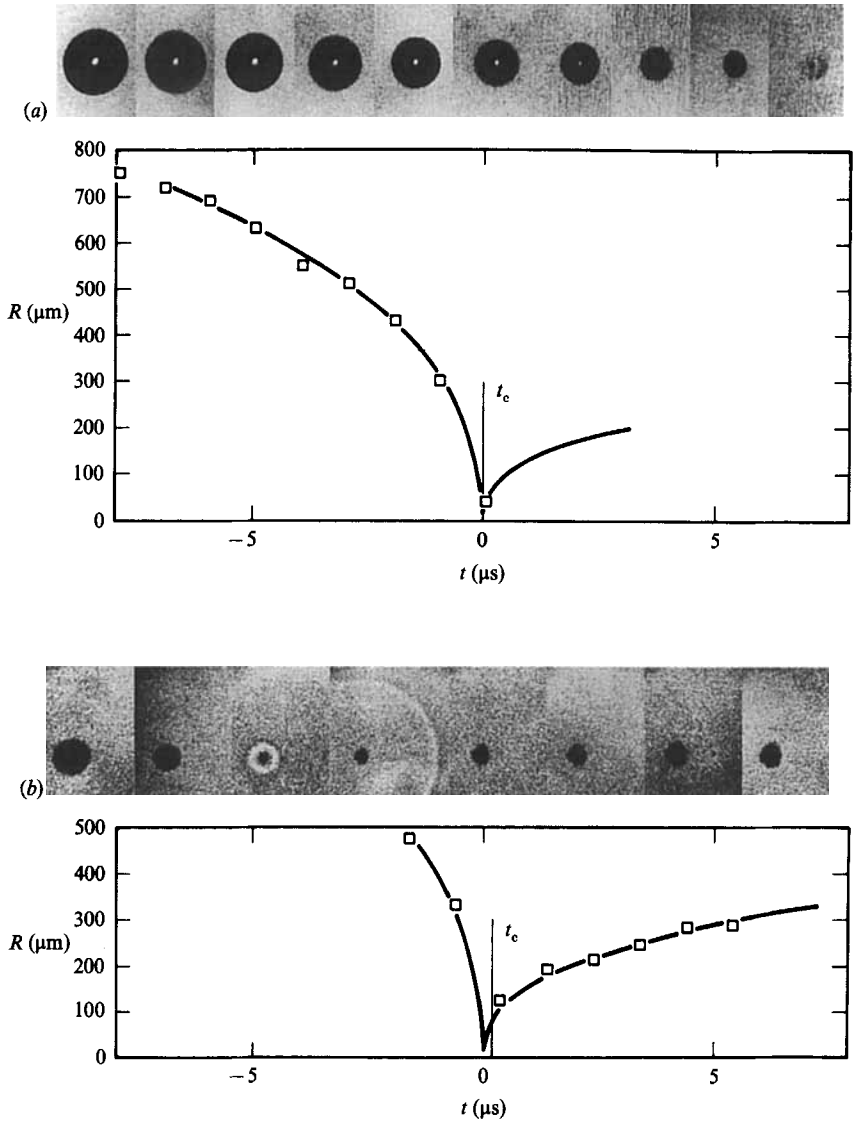

FIGURE 29. High-speed photographic series of spherical bubble collapse far from boundaries taken with the image converter camera at 1 million frame/s, and comparison of the corresponding radius values with numerical calculations based on Gilmore's theory. t_c is the instant of collapse obtained from the position of the acoustic transients on the photographs.

achieved by varying the associated velocity of the bubble wall, and the equilibrium radius of the bubble, i.e. the radius, where the pressure of the permanent gas inside the bubble equals the static pressure of the liquid. The instant t_c of collapse was experimentally obtained from the position of the acoustic transients on the photographs using the normal velocity of sound in water (1490 m/s; the exact velocity of the acoustic transient is not known, because of its shock-wave properties in the initial stage of propagation). Since in figure 29(*a*) the moment of exposure of the last frame is almost identical with t_c as well as with the time of collapse resulting from the numerically calculated curve, the radius value of 50 μm taken from the

photograph is identified with the minimum bubble size. An uncertainty is left, however, because the exposure time of 200 ns may cause a blurred image if during a short time the bubble is smaller than 50 μm. In figure 29(*b*) t_c does not correspond to the instant of collapse given by the theoretical curve, and in both figures 29(*a*) and 29(*b*) the minimum bubble size calculated numerically (4.9 μm in *a* and 6.8 μm in *b*) is much smaller than the experimental value. Obviously, the Gilmore theory does not properly model the final stage of the collapse. This might be due to its neglect of non-equilibrium condensation of the vapour inside the bubble and of heat conduction. Fujikawa & Akamatsu (1980) have taken these two factors into consideration, and have shown that in this case the bubble contracts slowly in the final stages of the collapse in comparison with the adiabatic case assumed in the Gilmore model. Moreover, the perfect sphericity assumed in theory is never completely fulfilled in reality, which leads to a weaker collapse than theoretically predicted.

3.4.3. *Bubble collapse near a solid boundary*

The solid boundary leads to a decrease of the amplitude of the pressure pulse caused by the first bubble collapse and to an increase of the pressure produced at the second collapse. In addition, the boundary causes a prolongation of the collapse time so that (3) does not hold any longer. The maximum bubble radius may still be determined from the collapse time, if the prolongation factor against Rayleigh's collapse time for the spherical collapse is known. The knowledge of the maximum bubble radius before the first collapse and after rebound makes it possible to calculate the bubble energy and the energy loss during collapse. The dependence of the prolongation factor k on the dimensionless distance γ between bubble and boundary was experimentally investigated by evaluating a large number of high speed photographic series of bubble dynamics. The result is shown in figure 30 together with a theoretical curve derived from a perturbation analysis by Rattray (see Plesset & Chapman 1971).

Figure 31 shows the pressure amplitude of the acoustic transient after the first bubble collapse as a function of γ. The pressure was normalized to a distance of 10 mm from the collapse centre. Since the sound emission during aspherical bubble collapse may be anisotropic, two series of measurements were performed with the pressure transducer placed above the bubble and the boundary in one series and beside the bubble in the other series. The average bubble radius was $R_{max} = 3.5 \pm 0.6$ mm in both cases. Thus, the pressure values for a certain γ-value may belong to bubbles of slightly different amplitudes. This partly masks the law governing the relationship between sound emission and the normalized distance γ. The importance of sound emission in damping the bubble oscillations for aspherical collapse can be estimated by relating the energy of the acoustic transient produced during the collapse to the energy loss of the bubble as shown in figure 32. The curves have been fitted to the measurement values in order to facilitate the comparison of both measurement series with different microphone positions.

Looking at figures 31 and 32, the strong decrease in sound emission for γ-values of about $\gamma = 0.9$ attracts attention. This behaviour was also observed by Naudé & Ellis (1961) and by Tomita & Shima (1986). It is due to the modification of the bubble collapse by jet and ring vortex formation discussed in §§3.1 and 3.2. For large γ-values, the collapse is almost spherical and the liquid jet does not emerge before the rebound of the bubble. Therefore, the liquid moves almost radially towards the collapse centre, leading to a violent collapse with strong sound emission. In the range around $\gamma = 0.9$, the jet appears before the bubble has achieved its minimum

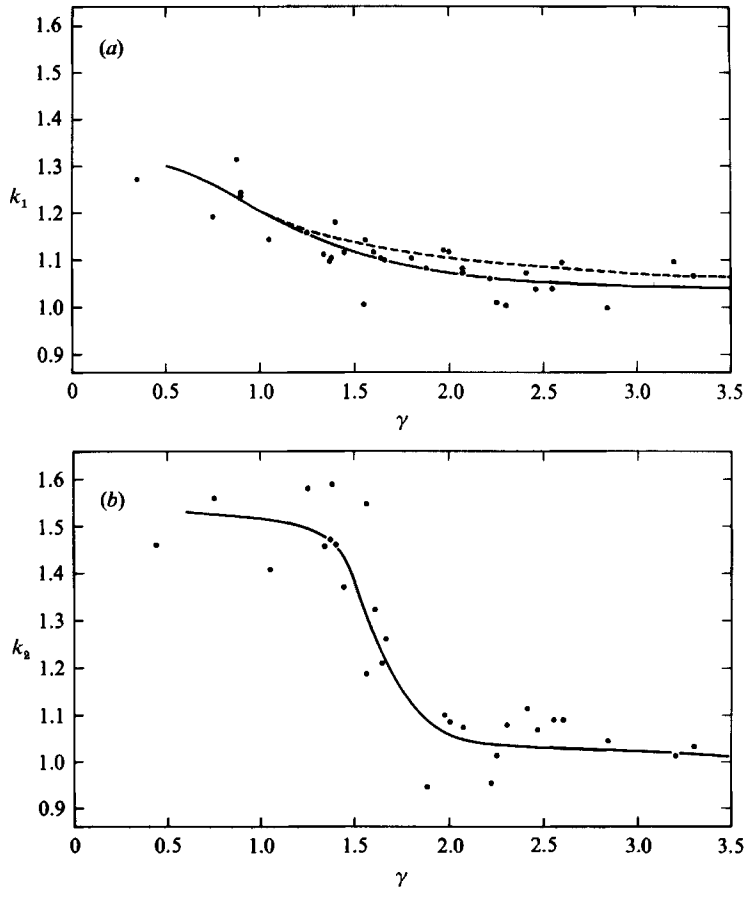

FIGURE 30. Prolongation factors k_1 and k_2 against the time for asymmetrical bubble collapse as a function of γ (*a*) for the first collapse and (*b*) for the second collapse: ----, theoretical curve derived by Rattray (see Plesset & Chapman 1971); ——, curve fitted to the values obtained experimentally. Figure taken from Vogel & Lauterborn (1988*b*).

extension. The jet penetrates the bubble wall at the side of the solid boundary, and during the last stages of the collapse a vortex ring with a hollow toroidal core consisting of gas and vapour is formed which moves towards the boundary. The kinetic energy of the radial flow into the bubble is thereby partly transformed into energy of rotation. Hence, the bubble contents becomes less compressed than in the case of large γ-values (see the comparison of minimum bubble sizes for both cases in figure 21*a* and *b*), and the sound emission is diminished. For $\gamma \to 0$, the sound emission increases again, although the jet is still formed very early during the collapse, similar to the case of $\gamma = 0.9$. However, if γ is very small, the bubble is nearly hemispherical and its centre can hardly move during collapse. Therefore, no pronounced vortex ring is developed in spite of the outward flow on the surface of the solid boundary following jet impact. The flow is directed towards the bubble centre for most parts of the bubble surface, as in the spherical collapse. This causes a strong compression of the bubble contents and the generation of an intense pressure pulse. Figure 32 shows that for $\gamma \leqslant 2.0$ the damping of the bubble oscillation is predominantly caused by mechanisms other than the emission of sound. Instead, damping is probably mainly due to viscosity and heat transport, which are

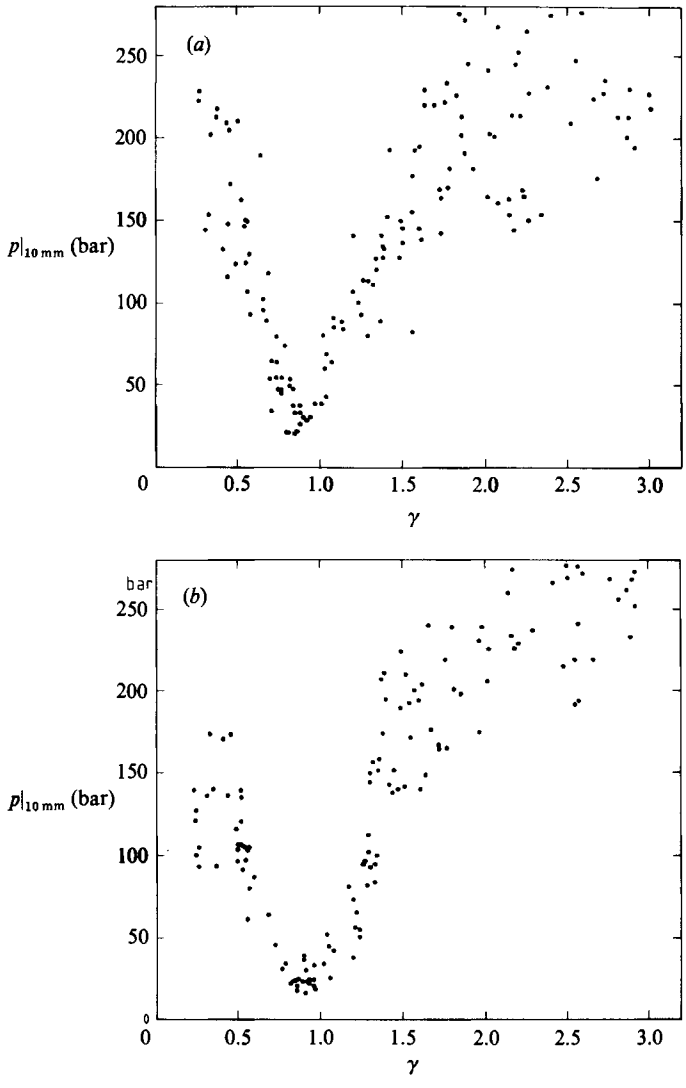

FIGURE 31. Pressure amplitude p after the first bubble collapse as a function of γ. The pressure values refer to a distance of 10 mm from the collapse centre. $R_{max} = 3.5 \pm 0.6$ mm. The hydrophone was placed (*a*) above and (*b*) beside the bubble. Figure adapted from Vogel & Lauterborn (1988*b*).

significant within this parameter range because of the turbulent jet flow and the ring vortex.

For $\gamma < 1.1$, this jet hits the solid boundary before the bubble reaches its minimum size, so that the pressure pulses due to jet impact and bubble rebound are generated at different times. Nevertheless, only one strong transient is registered by the hydrophone during bubble collapse. It is very likely that this is the transient emitted by the rebounding bubble. The pressure pulse produced at the site of the jet impact has to pass the cavitation bubble with a low acoustic impedance until it reaches the hydrophone. It is therefore strongly attenuated at the side where the liquid is, whereas the coupling to the solid wall is much better. The pulse from the rebounding bubble, however, is directly transmitted to the transducer by the liquid surrounding the bubble. This view is supported by holographic interferograms of shock-wave-

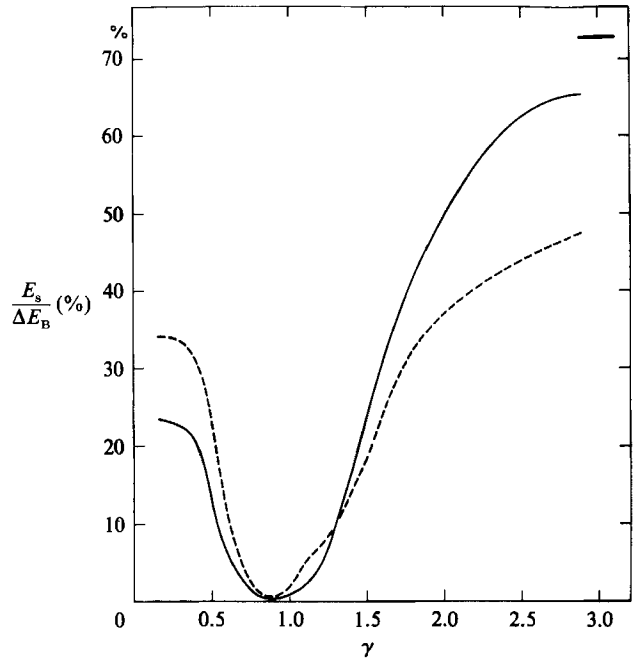

FIGURE 32. Fraction of the energy loss ΔE_B during the first bubble collapse which is converted into acoustic energy E_S, plotted versus γ. The average value for the spherical collapse is marked by the horizontal bar. ——, hydrophone placed above the bubble; ----, hydrophone placed beside the bubble. Figure taken from Vogel & Lauterborn (1988*b*).

induced bubble collapse on a transparent solid wall taken by Sanada *et al.* (1986). The interferograms show the pressure field in the liquid surrounding the bubble and in the solid wall, indicating strongly anisotropic sound emission. Our acoustic measurements thus only allow the determination of the pressure inside the collapsed cavitation bubble but not the impact pressure of the jet, even though the latter may locally be higher than the former (see also §3.5 below).

The highest pressure amplitudes at the solid boundary due to the compression of the bubble contents are achieved when γ is very small. One can infer from figure 31 that for $\gamma = 0.2$ and $R_{max} = 3.5$ mm the pressure amplitude after the first bubble collapse is about 150 bar at a distance of 10 mm from the collapse centre. This value is the average of the data from each hydrophone position. It is estimated from figure 7(*d*) that the minimum volume of the collapsed bubble corresponds to that of a bubble with a radius of about 0.6 mm. Calculation of the pressure value at this radius proceeding from the measured amplitude yields the value of 2.5 kbar for the maximum pressure inside the bubble and at the boundary. This result agrees well with the findings of Jones & Edwards (1960) (10 kbar for $\gamma = 0$ and $R_{max} = 4.9$ mm), but it is almost 17 times higher than the value reported by Tomita & Shima (1986) (150 bar for $\gamma = 0.2$ and $R_{max} = 3.5$ mm). The deviation can be explained by the fact that Tomita & Shima employed a pressure transducer with a rise time of 1 μs without considering the much shorter duration of the pressure pulses to be measured, whereas Jones & Edwards performed a dynamic calibration of their transducers.

3.5. *Cavitation erosion*

Our measurements have shown that the highest pressure amplitudes at the solid boundary due to the compression of the bubble contents are achieved for $\gamma \to 0$. In this case, moreover, there is no water film between bubble and boundary cushioning the impact of the liquid jet. Bubbles attached to the boundary thus have the largest damage potential. Nevertheless, from the measured and extrapolated jet velocities and pressure values some reasonable doubt arises about whether the action of a single isolated cavitation bubble collapsing in a liquid without additional flow will lead to erosion of hard metals. As discussed below, there is some evidence that only modifications of the bubble collapse by shock wave–bubble interaction or by a flow carrying the bubble will produce liquid jets with a velocity high enough to damage such materials.

The highest jet velocity observed in our study was 156 m/s for γ about 2.3. This value is obtained from figure 25(*a*) by identifying the tip of the jet with the lower bubble wall. In figure 25(*b*) with $\gamma < 2$ the velocity is 118 m/s. A reduction of jet velocity with decreasing γ was also found in the numerical studies by Plesset & Chapman (1971) (170 m/s for $\gamma = 1.5$, 130 m/s for $\gamma = 1.0$) and by Blake *et al.* (1986) (161 m/s for $\gamma = 2.0$, 110 m/s for $\gamma = 1.5$, 86 m/s for $\gamma = 1.0$, when a collapse in water under atmospheric pressure is assumed). We have shown in figure 20 that the second numerical model is a better approximation to real bubble dynamics than the first. Therefore, 86 m/s is a more realistic value for the jet velocity at $\gamma = 1.0$ than 130 m/s. Only for γ-values smaller than about 0.9 does the jet hit the solid wall without being decelerated by a water layer or being transformed into a ring vortex before the end of the first collapse (see §3.2). For estimating the damage capability of the jet we therefore have to presume a jet velocity of 100 m/s or less.

The water hammer pressure corresponding to a jet velocity of 100 m/s is about 1.5 kbar. Since, according to Lesser & Field (1983) and to Lush (1983), the pressure due to the impact of a liquid jet with a conical or round tip can be up to 2.9 times the water hammer pressure, it may reach about 4.5 kbar. This is in the same range as the pressure of 2.5 kbar achieved inside a collapsed cavity attached to the wall. Both values are close to the (static) Brinell hardness of, for example, 99% pure aluminium which is about 3 kbar (Wellinger & Gimmel 1963), but Lush (1983) found the dynamic hardness of 99% pure aluminium measured with a falling ball test to be about 13 kbar, and Tomita & Shima (1986) observed pitting of an indium specimen hit by a pressure-wave-induced jet only after the water hammer pressure was more than ten times the yield strength of indium. An initially spherical cavitation bubble should therefore probably hardly be able to erode aluminium or harder metals neither by jet impact nor by the pressure inside the collapsed bubble. On first sight, this seems to be contradictory to the results of Naudé & Ellis (1961) and Lush, Wood & Carpanini (1983) who observed small pits in aluminium below the centre of spark-produced bubbles. Their bubbles, however, were very large ($R_{\max} = 5$ mm), and pits could only be produced in a very small interval around $\gamma = 0.2$. Shutler & Mesler (1965) and Tomita & Shima (1986) found no central pits, but only a ring-shaped damage pattern located at the periphery of the collapsed bubble. Tomita & Shima pointed out that this could be explained by the interaction of the outward-flowing jet with the contracting cavity surface as a result of which microbubbles are produced. One can see in figure 7(*c*) with $\gamma = 0.75$ and in 7(*d*) with $\gamma = 0.34$ that for small γ-values the cavitation bubble reaches its minimum size about 50 μs after the jet has hit the boundary. This means that the microbubbles produced by the jet flow

shortly after their generation are struck and collapsed by a pressure pulse of about 2.5 kbar arising from the collapse of the main cavity. Thereby, probably much higher pressures are produced locally at the solid boundary. They may be well above the dynamic hardness of aluminium or other metals.

A similar interaction between bubbles and pressure pulses occurs on a larger scale during the collapse of cavity clouds in hydraulic cavitation and during extracorporeal shock wave lithotripsy. It has been reported by Tomita & Shima (1986) that a pressure pulse with an amplitude of 50 bar hitting a gas bubble produces jets with a velocity of 200–370 m/s. Dear & Field (1988) have observed jets with 400 m/s after a disk-shaped cavity was struck by a shock wave with a strength of 2.6 kbar. The respective impact pressures of the jet are 3–6 kbar, or even 9–18 kbar, if the tip of the jet has the appropriate shape. It is likely that the jets can be even faster when the acoustic transients interact with already collapsing cavitation bubbles rather than with gas bubbles. A pressure pulse with an amplitude of 50 bar necessary to induce the fast jets can be produced by the spherical collapse of a cavitation bubble with $R_{\max} = 3.5$ mm at a distance of 60 mm from the first bubble (see figure 28). This distance decreases to 30 mm if a slightly asymmetric collapse ($\gamma \to 1.5$) of the second bubble is assumed (see figure 31). Bubble–pressure pulse interactions as described above are very likely to occur in bubble clusters in hydrodynamic cavitation. They are probably also responsible for the damage due to liquid-jet impact observed recently by Coleman *et al.* (1987) and Delius *et al.* (1988) in experiments with an extracorporeal shock wave lithotripter. Each pressure pulse from a lithotripter consists of a peak with an amplitude of several hundred bar followed by a part with a negative pressure of about 100 bar. The negative pressure produces cavitation with both transient and stable bubbles. The stable bubbles are then collapsed by the leading edge of the following pressure pulse. Delius *et al.* have found damage structures explainable only by simultaneous jet impact at several adjacent sites. This has given evidence that the pits observed have not been caused by simple cavitation bubble collapse but by the simultaneous interaction of preformed bubbles with a pressure pulse.

Another mechanism that may influence the jet velocity is the deformation of the initial bubble shape by a flow around the bubble. We have discussed in §3.3. how the jet is linked to the bubble elongation developing during collapse. We found that a strong elongation of the bubble in the vertical direction, i.e. perpendicular to the solid boundary, causes a low velocity which for $\gamma > 1$ allows a counterjet to develop. Voinov & Voinov (1976) have theoretically investigated the consequences arising when a bubble detached from the wall is elongated in the horizontal direction at the stage of maximum bubble expansion. They found that at an elongation of only 10% the jet velocity is twice that in the case of an initially spherical bubble. Larger elongations lead to even higher jet velocities but also to a strong decrease of the liquid volume forming the jet. First experimental evidence for this theory can be found in the work of Kling & Hammitt (1972). They generated cavitation bubbles in a flow through a venturi with a velocity of 25 m/s under an ambient pressure of 2 bar. This led to an elongation of 15% parallel to the venturi walls (measured at maximum bubble expansion) for a bubble at $\gamma = 1.14$ and $R_{\max} = 2$ mm. The maximum jet velocity (taken from their figure 5) was about 300 m/s, and they reported an impact velocity of 120 m/s resulting in pits in an aluminium foil in spite of the water layer between bubble and boundary. The numerical calculations of Blake *et al.* (1986) for the no-flow case give a maximum jet velocity of 122 m/s for $\gamma = 1.0$ and an ambient pressure of 2 bar, and our measurements with $\gamma < 2$ (figure

25*b*) deliver a jet velocity of 167 m/s when the results are transformed to an ambient pressure of 2 bar. The jet velocity observed by Kling & Hammit (1972) for a bubble elongated 15% in the horizontal direction is thus twice as high as it would have been for an initially spherical bubble. A further confirmation of the acceleration of the jet due to bubble elongation is given by the results of Ellis & Starrett (1983). They reported that the impact pressure of liquid jets from bubbles elongated parallel to the solid boundary in a stagnation flow of 6 m/s is more than an order of magnitude higher than the pressure produced in the no-flow situation.

Thus there are two mechanisms that may enhance the damage capability of collapsing bubbles beyond the threshold of damage for stronger materials: (i) pressure pulses from adjacent collapsing bubbles; and (ii) a fluid flow leading to an elongation parallel to the boundary at the stage of maximum bubble expansion.

4. Conclusions

The dynamics of laser-produced cavitation bubbles near a solid boundary has been investigated by high-speed photography, time-resolved particle image velocimetry and acoustic measurements. The main results are as follows:

(i) Bubble collapse near a solid boundary is accompanied by the formation of a high-speed liquid jet toward the boundary. The jet flow leads to ring vortex formation after the first collapse for a relative distance γ between bubble and boundary larger than 1.5, and to ring vortex formation before the first collapse for γ-values of about 0.9. The ring vortex formation before the first bubble collapse causes a strong reduction of the sound emission during collapse.

(ii) From successive measurements of the velocity field of the fluid flow in the vicinity of the bubble, pathlines have been derived agreeing well with the results of numerical calculations. It was shown that the dynamical behaviour of the bubble is more accurately described by the numerical model of Blake *et al.* (1986) than by the model of Plesset & Chapman (1971) which does not include the growth phase of the bubble.

(iii) Counterjet formation disturbing the development of the principal jet has been found to be a common feature of bubble dynamics in the parameter range $2.0 \geqslant \gamma \geqslant 1.0$.

(iv) Sound emission is the main damping mechanism in spherical bubble collapse in water, where on average 73% of the energy loss of the bubble is due to the emission of an acoustic transient. It plays a minor part in the damping of aspherical bubble collapse, especially in the range of $1.3 \geqslant \gamma \geqslant 0.6$, where it contributes less than 10% to the energy loss of the bubble.

(v) The pressure profile of the acoustic transients has the form of an exponential impulse with a rise time of less than 10 ns. The duration of the pressure pulses (their width at half-maximum) has been found to be 20–30 ns at from 0.6 mm to 6 mm from the emission centre of the pulses.

(vi) During spherical bubble collapse, a maximum pressure of about 60 kbar is developed inside a bubble with $R_{\max} = 3.5$ mm. The highest pressure amplitudes at the solid boundary are produced when γ approaches zero. For $\gamma = 0.2$ and $R_{\max} = 3.5$ mm, the maximum pressure inside the bubble is about 2.5 kbar. This is about the same value as the estimated water hammer pressure resulting from jet impact on the boundary.

(vii) Jet formation seems to be the mechanism mainly responsible for cavitation erosion – but to fully realize the damage potential of the jet, one has to consider the

acceleration of jet formation by acoustic transients from adjacent bubbles and/or the change of jet velocity due to deviations from the spherical bubble form which may occur in a fluid flow.

The work reported here was financially supported by the Fraunhofer-Gesellschaft. The experiments with the rotating mirror camera were done at the Institut für den Wissenschaftlichen Film in Göttingen.

REFERENCES

ARON-ROSA, D., ARON, J. J., GRIESEMANN, M. & THYZEL, R. 1980 Use of the neodymium:YAG laser to open the posterior capsule after lens implant surgery: a preliminary report. *Am. Intraocul. Implant Soc. J.* **6**, 352–354.

BENJAMIN, T. B. & ELLIS, A. T. 1966 The collapse of cavitation bubbles and the pressure thereby produced against solid boundaries. *Phil. Trans. R. Soc. Lond.* A **260**, 221–240.

BLAKE, J. R. & GIBSON, D. C. 1981 Growth and collapse of a vapour cavity near a free surface. *J. Fluid Mech.* **111**, 123–140.

BLAKE, J. R., TAIB, B. B. & DOHERTY, G. 1986 Transient cavities near boundaries. Part 1. Rigid boundary. *J. Fluid Mech.* **170**, 479–497.

BREWER, R. G. & RIECKHOFF, K. E. 1964 Stimulated Brillouin scattering in liquids. *Phys. Rev. Lett.* **13**, 334–336.

CAROME, E. F., MOELLER, C. E. & CLARK, N. A. 1966 Intense ruby-laser-induced acoustic impulse in liquids. *J. Acoust. Soc. Am.* **40**, 1462–1466.

CHAHINE, G. L. & GENOUX, P. G. 1983 Collapse of a cavitating vortex ring. *Trans. ASME* I: *J. Fluids Engng* **105**, 400–405.

COLE, R. H. 1948 *Underwater Explosions.* Princeton University Press.

COLEMAN, A. J., SAUNDERS, J. E., CRUM, L. A. & DYSON, M. 1987 Acoustic cavitation generated by an extra corporeal shockwave lithotripter. *Ultrasound Med. Biol.* **13**, 69–76.

DEAR, J. P. & FIELD, J. E. 1988 A study of the collapse of arrays of cavities. *J. Fluid Mech.* **190**, 409–425.

DELIUS, M., MÜLLER, M., VOGEL, A. & BRENDEL, W. 1988 Shock waves and cavitation. In *Biliary Lithotripsy* (ed. J. Ferrucci, J. Burhenne & M. Delius). Chicago: Yearbook.

EBELING, K. J. 1978 Zum Verhalten kugelförmiger, lasererzeugter Kavitationsblasen in Wasser. *Acustica* **40**, 229–239.

ELLIS, A. T. & STARRET, J. E. 1983 A study of cavitation bubble dynamics and resultant pressures on adjacent solid boundaries. In *Proc. 2nd Intl Conf. on Cavitation*, paper C 190/83. I. Mech. E, London.

ESIPOV, I. B. & NAUGOL'NYKH, K. A. 1972 Expansion of a spherical cavity in a liquid. *Soviet Phys. Acoust.* **18**, 194–197.

FANKHAUSER, F., ROUSSEL, P., STEFFEN, J., VAN DER ZYPEN, E. & CHRENKOVA, A. 1981 Clinical studies on the efficiency of high power laser radiation upon some structures of the anterior segment of the eye. *Intl Opthalmol.* **3**, 129–139.

FUJIKAWA, S. & AKAMATSU, T. 1980 Effects of the non-equilibrium condensation of vapour on the pressure wave produced by the collapse of a bubble in a liquid. *J. Fluid Mech.* **97**, 481–512.

GILMORE, F. R. 1952 The growth or collapse of a spherical bubble in a viscous compressible fluid. *Cal. Tech. Inst. Rep.* 26–4.

HENTSCHEL, W. & LAUTERBORN, W. 1982 Acoustic emission of single laser-produced cavitation bubbles and their dynamics. *Appl. Sci. Res.* **38**, 225–230.

HICKLING, R. & PLESSET, M. S. 1964 Collapse and rebound of a spherical bubble in water. *Phys. Fluids* **7**, 7–14.

HINSCH, K. & BRINKMEYER, E. 1976 Investigation of very short cavitation shock waves by coherent optical methods. *High Speed Photography*, SPIE Vol. 97, pp. 166–171. Toronto.

JONES, I. R. & EDWARDS, D. H. 1960 An experimental study on the forces generated by the collapse of transient cavities in water. *J. Fluid Mech.* **7**, 596–609.

KLING, C. L. & HAMMITT, F. G. 1972 A photographic study of spark-induced cavitation bubble collapse. *Trans. ASME* D: *J. Basic Engng* **94**, 825–833.

KUCERA, A. & BLAKE, J. R. 1988 Computational modelling of cavitation bubbles near boundaries. In *Computational Techniques and Applications CTAC-87* (ed. J. Noyce & C. Fletcher), pp. 391–400. North-Holland.

LAUTERBORN, W. 1974 Kavitation durch Laserlicht. *Acustica* **31**, 51–78.

LAUTERBORN, W. 1982 Cavitation bubble dynamics – new tools for an intricate problem. *Appl. Sci. Res.* **38**, 165–178.

LAUTERBORN, W. & BOLLE, H. 1975 Experimental investigations of cavitation-bubble collapse in the neighbourhood of a solid boundary. *J. Fluid Mech.* **72**, 391–399.

LAUTERBORN, W. & HENTSCHEL, W. 1985 Cavitation bubble dynamics studied by high speed photography and holography: Part One. *Ultrasonics* **23**, 260–268.

LESSER, M. B. & FIELD, J. E. 1983 The impact of compressible liquids. *Ann. Rev. Fluid Mech.* **15**, 97–122.

LUSH, P. A. 1983 Impact of a liquid mass on a perfectly plastic solid. *J. Fluid Mech.* **135**, 373–387.

LUSH, P. A., WOOD, R. J. K. & CARPANINI, L. J. 1983 Pitting in soft aluminium produced by spark-induced cavitation bubbles. In *Proc. 6th Intl Conf. on Erosion by Liquid and Solid Impact* (ed. J. E. Field & Corney), paper 5. Cavendish Laboratory, Cambridge.

MAXWORTHY, T. 1974 Turbulent vortex rings. *J. Fluid Mech.* **64**, 227–239.

MAXWORTHY, T. 1977 Some experimental studies of vortex rings. *J. Fluid Mech.* **81**, 465–495.

NAUDÉ, C. F. & ELLIS, A. T. 1961 On the mechanism of cavitation damage by nonhemispherical cavities collapsing in contact with a solid boundary. *Trans. ASME* D: *J. Basic Engng* **83**, 648–656.

NISHIYAMA, T. & AKAIZAWA, M. 1979 Pressure waves produced by the collapse of a spherical bubble. *Technol. Rep. Tohoku Univ.* **44**, 579–602.

PLESSET, M. S. 1974 Bubble dynamics and cavitation erosion. In *Proc. Symp. on Finite-Amplitude Wave Effects in Fluids, IPC Science and Technology, Guildford* (ed. L. Bjørnø), pp. 203–209.

PLESSET, M. S. & CHAPMAN, R. B. 1971 Collapse of an initially spherical vapour cavity in the neighbourhood of a solid boundary. J. Fluid Mech. **47**, 283–290.

RADEK, U. 1972 Kavitationserzeugte Druckpulse und Materialzerstörung. *Acustica* **26**, 270–283.

RAYLEIGH, LORD 1917 On the pressure developed in a liquid during the collapse of a spherical cavity. *Phil. Mag.* **34**, 94–98.

REICHEL, E., SCHMIDT-KLOIBER, H., SCHÖFFMANN, H., DOHR, G. & EHERER, A. 1987 Interaction of short laser pulses with biological structures. *Optics Laser Technol.* **19**, 40–44.

SANADA, N., IKEUCHI, J., TAKAYAMA, K. & ONODERA, O. 1986 Interaction of an air bubble with a shock wave generated by a micro-explosion in water. *Proc. Intl Symp. on Cavitation. Sendai, Japan*, pp. 67–72.

SHUTLER, N. D. & MESLER, R. B. 1965 A photographic study of the dynamics and damage capabilities of bubbles collapsing near solid boundaries. *Trans. ASME* D: *J. Basic Engng.* **87**, 511–517.

STEINER, R. (ed.) 1988. Laserlithotripsy. *Proc. 1st Intl Symp. on Laser Lithotripsy Oct. 1987 in Ulm.* Springer.

STEPP, H., HOFBAUER, E., SEEBERGER, M. & UNSÖLD, E. 1985 Fast pressure measurements on shock waves intraocularly generated by picosecond Nd: YAG-laser pulses. *Laser in der Medizin und Chirurgie* **1**, 151–154.

STRUBE, H. W. 1971 Numerische Untersuchungen zur Stabilität nicht-sphärischer schwingender Blasen. *Acustica* **25**, 289–303.

TESLENKO, V. S. 1980 Experimental investigation of bubble collapse at laser-induced breakdown in liquids. In *Cavitation and Inhomogeneities in Underwater Acoustics* (ed. W. Lauterborn), pp. 30–34. Springer.

TOMITA, Y. & SHIMA, A. 1986 Mechanism of impulsive pressure generation and damage pit formation by bubble collapse. *J. Fluid Mech.* **169**, 535–564.

VOGEL, A., HENTSCHEL, W., HOLZFUSS, J. & LAUTERBORN, W. 1986 Cavitation bubble dynamics and acoustic transient generation in ocular surgery with pulsed Nd: YAG-lasers. *Ophthalmology* **93**, 1259–1269.

VOGEL, A. & LAUTERBORN, W. 1985 Ein Raumfrequenzfilterungsverfahren zur Untersuchung der Strömungsverhältnisse in der Umgebung von Kavitationsblasen. *Optik* **69**, 176–179.

VOGEL, A. & LAUTERBORN, W. 1988*a* Time resolved particle image velocimetry applied to the investigation of cavitation bubbles. *Appl. Opt.* **27**, 1869–1876.

VOGEL, A. & LAUTERBORN, W. 1988*b* Acoustic transient generation by laser-produced cavitation bubbles near solid boundaries. *J. Acoust. Soc. Am.* **84**, 719–731.

VOINOV, O. V. & VOINOV, V. V. 1976 On the process of collapse of a cavitation bubble near a wall and the formation of a cumulative jet. *Soviet Phys. Dokl.* **21**, 133–135.

VYAS, B. & PREECE, C. M. 1976 Stress produced in a solid by cavitation. *J. Appl. Phys.* **47**, 5133–5138.

WELLINGER & GIMMEL 1963 *Werkstofftabelle der Metalle*, p. 182. Stuttgart: Alfred Kröner.